Symposium on Materials Science

Mátraháza, Hungary, October 9-11, 2024

Editor:
Miklós Fried
Department of Microelectronics and Technology, Óbuda University
2025

ISBN 978-963-449-376-1

Organizing and Programme Committee:

ISBN 978-963-449-376-1

Table of contents

Zoltán Lábadi, Noor Taha Ismaeel, Peter Petrik, Miklós Fried: *Optimization of SnO2/ZnO Films for Electrochromic Coloration Efficiency* 7

Dániel Olasz, György Sáfrán, Miklós Serényi: *A guide to the reactive HiPIMS co-sputtering of Y and Ti* 11

Dávid Kovács, András Deák, Dániel Zámbó: *Spatial distribution of photoexcited electrons and holes in Cu2O/Au multicomponent nanoparticles* 16

Apoko S. Omondi, Dávid Kovács, András Deák and Dániel Zámbó: *On the inevitable role of shape in engineering porous multimetallic nanoparticles for catalytic applications* 21

Berhane Nugusse, György Juhász, Csaba Major, Péter Petrik, Sándor Kálvin, Zoltán György Horváth, Miklós Fried: *Optical calibration of the ellipsometric mapping tool from cheap parts* 26

N. Nagy: *Determination of solid-liquid adhesion work in a direct and absolute manner by the Capillary Bridge Probe* 33

D. Mukherjee, K. Kertész, Z. Zolnai, Z. Kovács, A. Deák, A. Pálinkás, Z. Osváth, D. Olasz, A. Romanenko, M. Fried, S. Burger, G. Sáfrán, P. Petrik: *Optimized Sensing on Gold Nanoparticles Created by Graded-Layer Magnetron Sputtering and Annealing* 36

The Symposium

Lecturer: Dániel Zámbó

Lecturer: András Deák

Lecturer: Géza Szántó

Lecturer: Dániel Olasz

Lecturer: Anita Horváth

Lecturer: Bálint Medgyes

Lecturer: Dávid Kovács

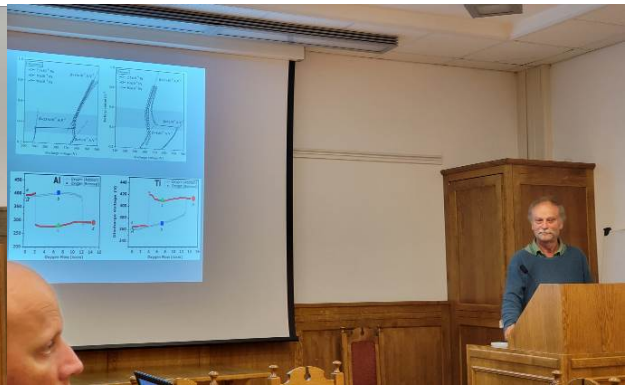

Lecturer: György Sáfrán

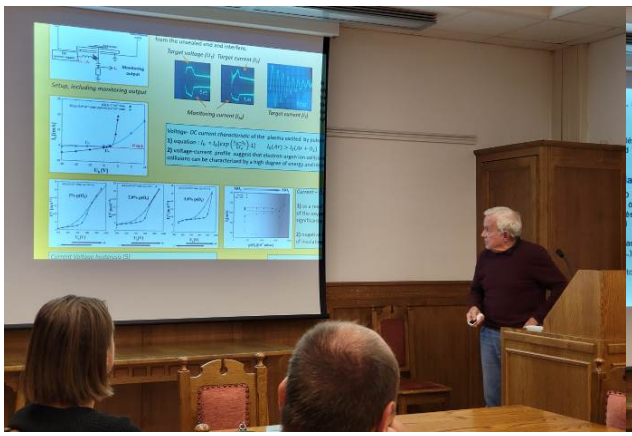

Lecturer: Miklós Serényi

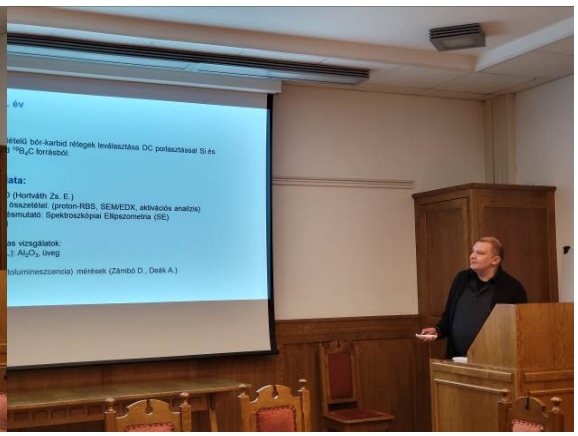

Lecturer: Zsolt Zolnai

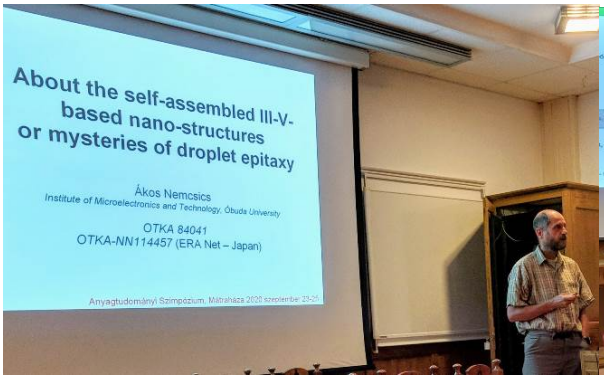

Lecturer: Ákos Nemcsics

Lecturer: Marcell Gajdics

Lecturer: Miklós Fried

Lecturer: Péter Petrik

Optimization of SnO_2/ZnO Films for Electrochromic Coloration Efficiency

Zoltán Lábadi[1], Noor Taha Ismaeel[1,2], Peter Petrik[1,3], Miklós Fried[1,2]

[1]Institute of Technical Physics & Materials Science, Centre for Energy Research, Konkoly-Thege Rd. 29-33, Budapest 1121, Hungary

[2]Institute of Microelectronics and Technology & Doctoral School on Materials Sciences and Technologies, Óbuda University, Budapest, Hungary

[3]Department of Electrical Engineering, University of Debrecen, Debrecen, Hungary

Electrochromic applications for metal oxides, such as smart windows and displays, have been widely studied recently. Electrochromic films decrease the extra absorption of heat in buildings. The electrochromic process is based on a reversible redox process and characterized by coloration efficiency (CE). Transition metal (titanium, tungsten, nickel, vanadium, molybdenum and others) oxide films are the most interesting and most widely studied materials for this purpose. [1] Nevertheless, relatively few publications have studied the possible advantages (higher CE) of the mixtures of different metal oxides as electrochromic materials. The change in light absorption for the same electric charge represents the electrochromic effectiveness, and it can be higher in mixed metal oxide layers.

Spectroscopic Ellipsometry (SE) has been used as an investigation method for combinatorial or pure materials since it is a cost-effective, non-destructive and fast method for the mapping of mixed oxide layers. A thickness map and a composition map have been achieved by the developed optical models of the sample layers.

The objective of this work was to determine the CE and to investigate the electrochromic effectiveness of SnO_2-ZnO mixed layers in the full compositional range. Mixed oxide layers were prepared by reactive DC magnetron sputtering. It should be noted that we apply a combinatorial approach for composition-graded layer deposition to allow study samples chosen from a full and continuous $SnO_{2(x)} - ZnO_{(1-x)}$ composition range. The deposited films were characterized using spectroscopic ellipsometry (SE), Scanning Electron Microscopy (SEM) with Energy-Dispersive X-ray Spectroscopy (EDS) and coloration efficiency (CE) measurements. We expected that mixing metal oxides with different sizes in films can enhance the CE.

Metallic Sn and Zn targets were placed separately from each other, and indium–tin-oxide (ITO)-covered glass and Si-probes on a glass substrate (30 cm × 30 cm) were moved under the two separated targets (Sn and Zn) in a reactive argon–oxygen (Ar-O_2) gas mixture (see Figure 1). The tin-zinc oxide layers were deposited onto ITO-covered 100 × 25 mm glass surfaces. Layer depositions were carried out by reactive sputtering in an (Ar + O_2) gas mixture at a ~2×10^{-4} Pa base pressure and at a ~10^{-1} Pa process pressure. The target–substrate working distance was 6 cm. Volumetric flow rates of 30 sccm/s Ar and 70 sccm/s O_2 were applied in the magnetron sputtering chamber. The plasma powers of the Sn and Zn metal targets were set to 800 and 1000 W, respectively. The samples were moved back and forth at a 25 cm/s walking speed between the Sn and Zn targets, and a mixed oxide film was deposited onto the ITO surface. A 5 min cooling interruption was applied after every 50 walking cycles.

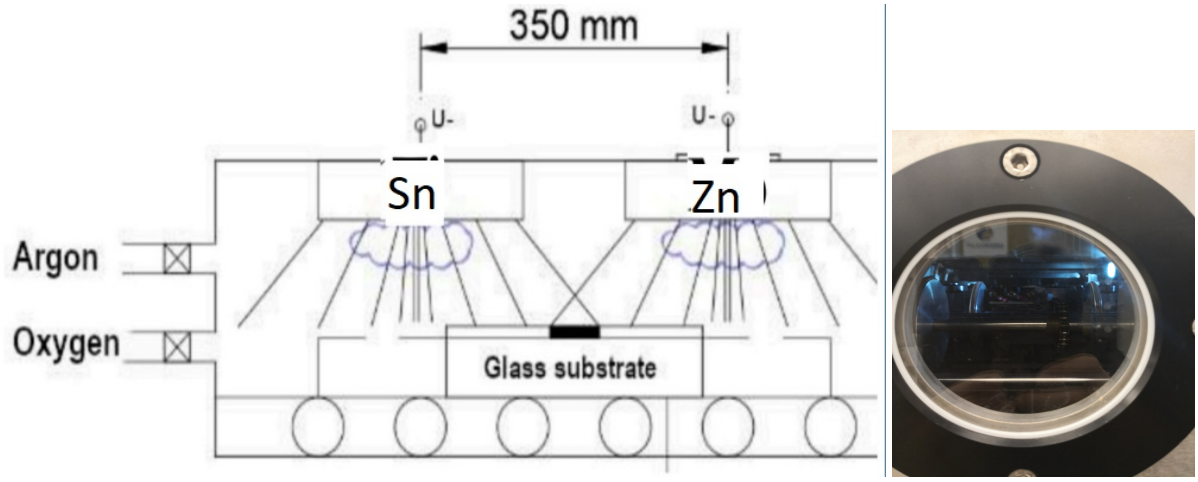

Figure 1. Target arrangement for combinatorial deposition and an insight into the chamber

Coloration Efficiency η is given by the following equation:

$$\eta(\lambda) = \frac{\Delta OD(\lambda)}{q/A} = \frac{\ln\left(\frac{T_b}{T_c}\right)}{Q_i}$$

where Q_i is the electrical charge inserted into the electrochromic material per unit area, ΔOD is the change in optical density, T_b is the transmittance in the bleached state, and T_c is the transmittance in the colored state. The unit of CE is cm^2/C (square centimeters per Coulomb).

The CE was determined in a transmission electrochemical cell (see Figure 2). The cell was filled with 1 M lithium perchlorate ($LiClO_4$)/propylene carbonate electrolyte. A 5 mm width masked (Sn-Zn oxide-free) ITO strip of the slides remained above the liquid level, allowing direct electric contact with the cell. A Pt wire counter electrode was placed into the electrolyte alongside a reference electrode. This arrangement was a fully functional electrochromic cell. The applied current was controlled through the cell using a Farnell U2722 Source Measurement Unit (SMU). A constant current was applied through coloration and bleaching cycles of the electrochromic layer, and simultaneous spectral transmission measurements were performed by using a Woollam M2000 spectroscopic ellipsometer in transmission mode.

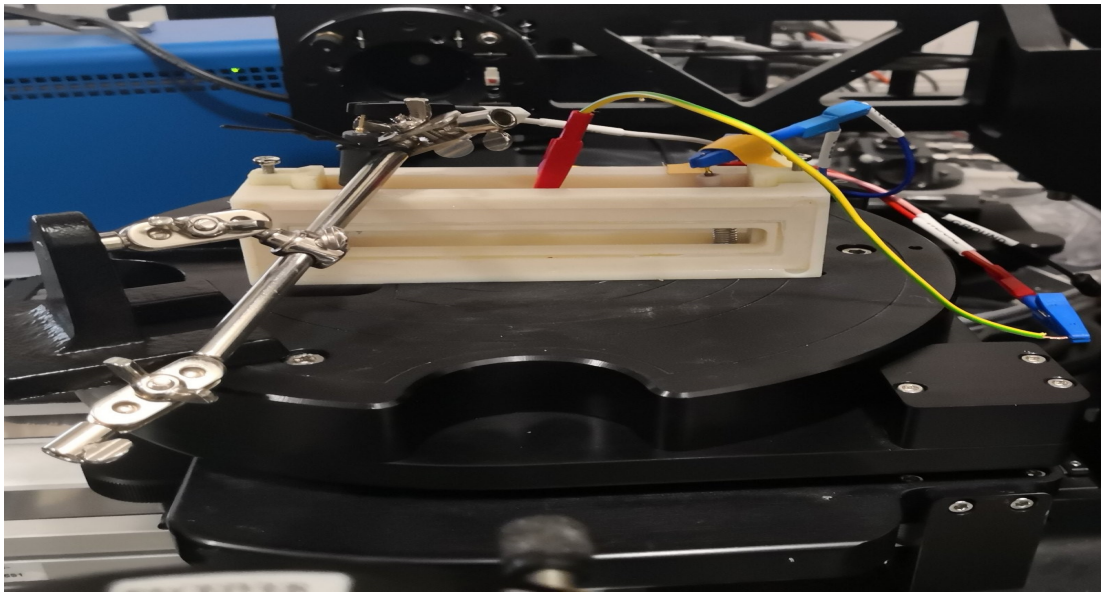

Figure 2: Setup for transparency measzremebnt during coloration – bleach cycles

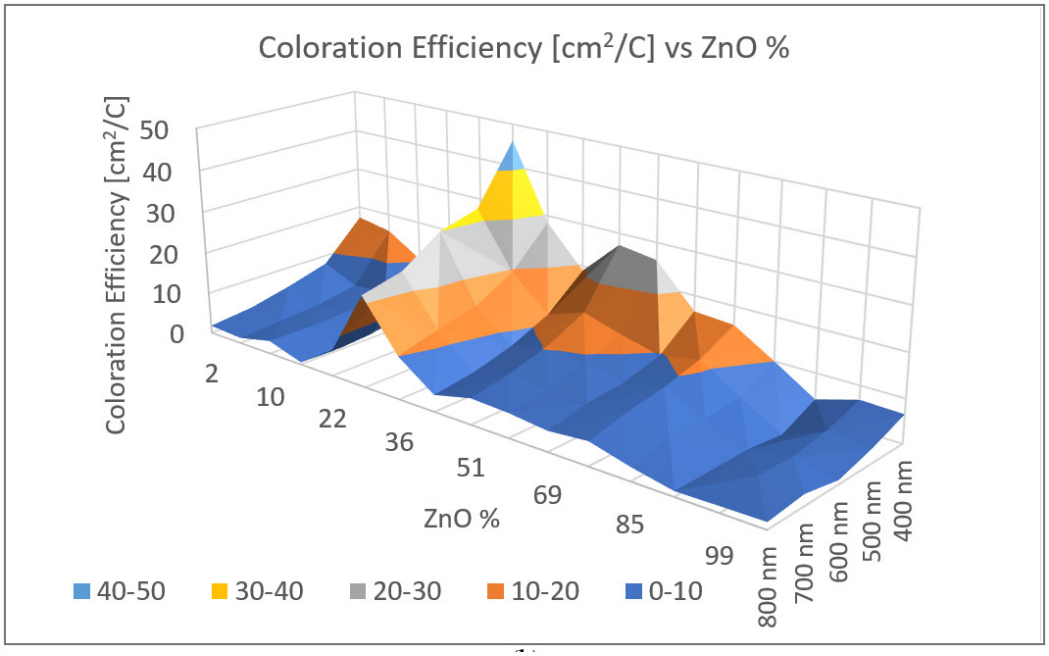

Figure 3: Three-dimensional diagram of CE data of SnO_2-ZnO vs. Zn % for wavelengths from 400 to 800 nm in visible spectral range.

Figure 3 shows the 3D representation of the calculated CE data as a function of the ZnO fraction of the film and the wavelength. Individual points were calculated from the average of three independent measurements. The error is estimated to be 3%, calculated based on the accuracy of sample positioning in the measuring cell and the spot size of the optical beam.

The CE maximum was found to be 29% Zn for each wavelength between 20 and 50 cm2/C. This 29% is very close to the optimum value of 30% in the case of the TiO2-SnO2 mixture which was investigated in our earlier paper [2]. We expected that mixing metal atoms with different diameters in the layers can enhance the CE. This (70–30)% mixture of different metal oxides seems to be the optimum for Li-diffusion in these sputtered materials.

The influence of mixing metal atoms with different diameters in the layers on EC behavior can be attributed to several factors. Mixing can create new pathways for charge carriers, enhancing the overall electrical conductivity. This increased conductivity can support faster ion intercalation and deintercalation processes, causing quicker color changes. Mixing can alter the electronic structure of the layer, affecting the way it absorbs and transmits light. These factors can explain the enhanced CE values [3]

[1] Granqvist, C.G. Handbook of Inorganic Electrochromic Materials, Elsevier: Amsterdam, The Netherlands, (1995)

[2] Noor, Taha Ismaeel ; Lábadi, Zoltán ; Petrik, Peter ; Fried, Miklós, Investigation of Electrochromic, Combinatorial TiO2-SnO2 Mixed Layers by Spectroscopic Ellipsometry Using Different Optical Models, Materials 2023, 16(12), 4204.

[3] Lábadi, Zoltán ; Ismaeel, Noor T. ; Petrik, Péter ; Fried, Miklós, Compositional Optimization of Sputtered SnO2/ZnO Films for High Coloration Efficiency, INTERNATIONAL JOURNAL OF MOLECULAR SCIENCES 25 : 19 Paper: 10801 , 11 p. (2024)

Acknowledgement:

Support of Hungarian Sci.Research Fund NKFIH OTKA K 143216, 146181 and TKP2021-EGA-04 is acknowledged.

A guide to the reactive HiPIMS co-sputtering of Y and Ti

Dániel Olasz[1,2], György Sáfrán[1], Miklós Serényi[1]

[1] Institute for Technical Physics and Materials Science,
HUN-REN Centre for Energy Research, H-1121, Budapest, Hungary

[2] Department of Materials Physics, Eötvös Loránd University,
Pázmány Péter Sétány 1/A, 1117, Budapest, Hungary

Introduction

Y-Ti-O ternary thin layer system has been widely studied [1] due to its microstructure, material properties and variety of applications, such as: in oxide dispersion-strengthened (ODS) alloys [2], resistance to radiation damage [3], nuclear waste management [4], photocatalyst [5]. Although high-power impulse magnetron sputtering (HiPiMS) technology is well suited for reactive sputtering of metallic targets to deposit metal oxide and nitride layers, finding the optimal sputtering parameters for Y and Ti targets with completely different behavior in the same reactive environment can be exciting [6]. This is greatly challenging to deposit a variable concentration Y- and Ti oxide layer, which allows the high throughput comprehensive characterization of microstructure and materials properties of the Y-Ti-O layer system.

Experimental

For the sputter deposition of the thin layers we used Ti and Y targets of 2 inch diameter from Kurt J. Lesker Company with 99.995 % and 99.9 % purity, respectively. For deposition a pair of HiPSTER 1 HiPIMS power supply unit by Ioanautics AB (Linköping, Sweden) was applied with the following specifications: max. output power 1 000 W, max. output peak voltage 1 000 V, max. output peak current 100 A, 1 to 10 000 Hz pulse frequency range and pulse duration range of 3.5 to 1 000 µs. The target to substrate distance was 10 cm during sputtering, that was carried out in an ultra-high vacuum (UHV) environment, with a base pressure of $2 * 10^{-8}$ mbar. The reactive O_2 gas flow is controlled by an EL-FLOW Prestige mass flow meter (Bronkhorst High-Tech) while the Ar working gas was introduced by a needle valve. The micro-combinatorial sample preparation method [7,8] was used to deposit a Y-Ti-O ternary layer of variable composition in the range of 5-95 at% Ti and Y content.

Results and discussion

The first characteristics that reveal significant differences in the behavior of the two targets are obtained by measuring the voltage as a function of the plasma current. The current can be measured through an electrode protruding into the discharge, which is inserted after the substrate has been separated from the base plate. The measured voltage-current characteristics (Figure 1) of the discharge differs significantly from the generally accepted Westwood equation $I=(U-U_o)^2$ [9] ; a "kink" appears as voltage increases. This is attributed to the secondary electron emission of the oxide layer formed on the target surface. The secondary electron emission of Ti oxide is lower than that of

pure Ti metal. On the contrary, Y-oxide emits more electrons than metallic Y. It is puzzling to find the common vacuum conditions for the deposition of oxide layers with materials behaving so differently. At the same time, one should both avoid the targets poisoning and control the ratio of Y to Ti in the sputtered layer over a wide range.

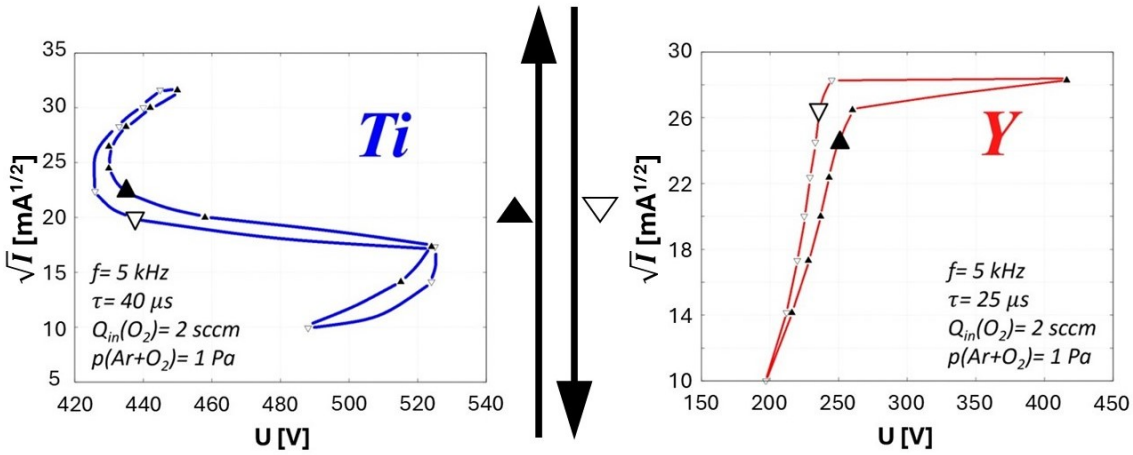

Figure 1: *Voltage-current characteristics for reactive sputtering of Ti and Y. (Filled symbols indicate data obtained at increasing current, empty symbols indicate data obtained at decreasing current.)*

Another significantly different behavior of Y and Ti is shown by the hysteresis which is typical for reactive sputtering, observed when the oxygen inflow is continuously changed. Figure 2a shows the very different nature of the Y and Ti manifested by the reversal in direction of hysteresis between the target voltage and the oxygen inflow.

According to our solution to prevent the yttrium target from being poisoned in the oxygen atmosphere common for both targets, the oxygen inlet was pulsed: a 4 s 2.5 sccm O_2 injection period was followed by a 2 s 0.5 sccm O_2 injection period, and these were repeated continuously (Figure 2b). The pulsation could be read off the pressure gauge during sputtering, indicating that the pulsation was slow enough to cause a noticeable pressure fluctuation. As a result, the oxidation state (oxide coverage) of the targets surface changed periodically; during one period, the hysteresis region shown in Figure 2a is drawn out. However, this change is fast enough that the oxide coverage characterizing the state of the targets can be considered constant on average. Conceptually, the target oscillates between the metallic and oxide branches of the hysteresis, which results in a virtual working point for sputtering and can provide ideal conditions for the deposition of a stoichiometric Y-Ti-O layer.

To ensure that the two components, Y and Ti, were present in the deposited oxide layer in the planned proportions, the targets were individually subjected to series of electrical pulses. The atomic ratios of Y and Ti are determined by the number of pulses, assigned to each targets, in the bursts (Figure 3). This solution was developed because of the nonlinearity of the current-voltage characteristics of the targets, as the usual increasing power - increasing amount of material deposition does not work due to the kinks. .However, the amount of material deposited is proportional to the number of pulses in the series.

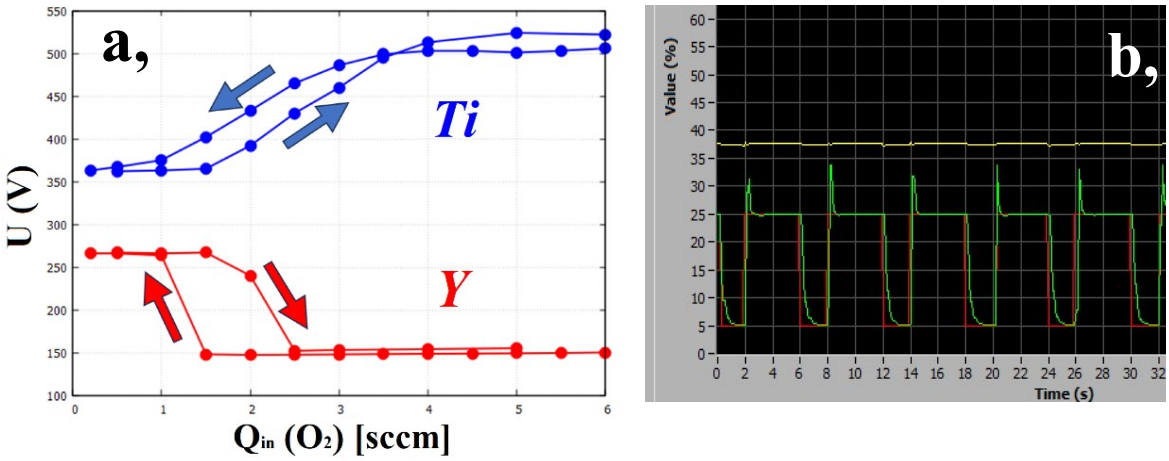

Figure 2: a, *Voltage versus O_2 inflow hysteresis for Y and Ti.* ***b,*** *Pulsed O_2 inflow as a function of time. Red curve corresponds to the planned O_2 inflow, while the green curve corresponds to the measured one.*

By increasing the number of pulses at one target and decreasing the number of pulses at the other target, a continuous change in concentration in the deposited layer can be achieved. The pulses are short enough in time and high enough in frequency relative to the time of flight in the recipient that the deposited layer has a homogeneous distribution of material (Figure 4).

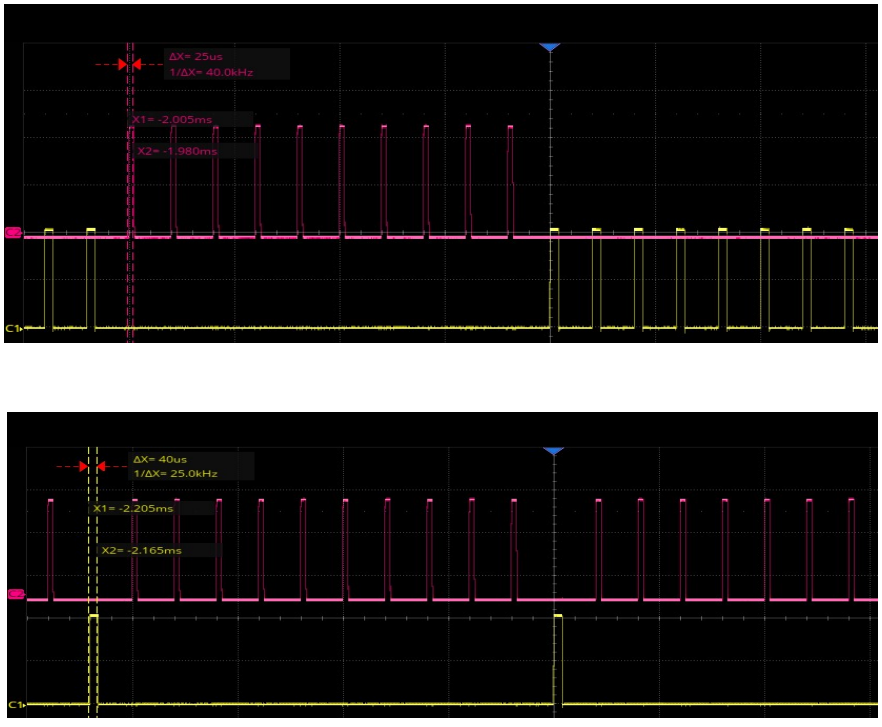

Figure 3: *Applied bursts on the Y (red curve) and Ti (yellow curve) targets. As illustrated by the upper and lower images, composition change is evoked by varying the numbers of bursts: a decline in the number of Ti bursts leads to an Y-enrichment of the deposited layer.*

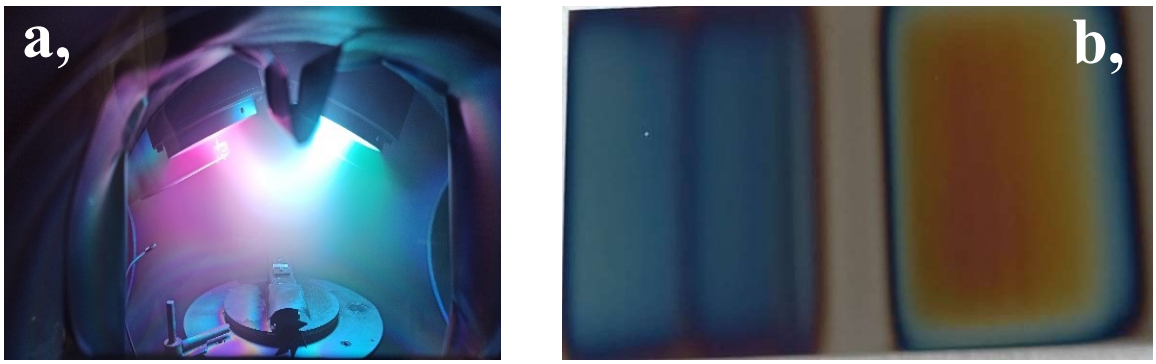

Figure 4: a, *Photograph of the chamber during simultaneous deposition of Y and Ti under pulsed oxygen inlet.* ***b,*** *Combinatorial Y-Ti-O layer deposited with varying Y and Ti concentrations along the 25 mm Si slab.*

Acknowledgement:

Support of Hungarian Sci.Research Fund OTKA, grant No. K143216 is acknowledged. Project no. C1792954 has been implemented with the support provided by the Ministry of Culture and Innovation of Hungary from the National Research, Development and Innovation Fund, financed under the KDP-2021 funding scheme.

References:

[1] D. Olasz, V. Kis, I. Cora, M. Németh, G. Sáfrán: High-Throughput Micro-Combinatorial TEM Phase Mapping of the DC Magnetron Sputtered $Y_xTi_{1-x}O_y$ Thin Layer System. *Nanomaterials* **2024**, 14, 925. https://doi.org/10.3390/nano14110925

[2] Y. Cai, L. Wang, J. Li, M. Yang, Q. Feng, T. Liu: Influences of adding $Y_2Ti_2O_7$ and $HfH_{1.98}$ nanoparticles on the microstructure and mechanical properties of oxide dispersion strengthen steels. *Mater. Charact.* **2023**, 202, 113040. https://doi.org/10.1016/j.matchar.2023.113040

[3] P. Song, D. Morrall, Z. Zhang, K. Yabuuchi, A. Kimura: Radiation responce of ODS ferritic steels with different oxide particles under ion-irradiation at 550 °C. *J. Nucl. Mater.* **2018**, 502, 76-85. https://doi.org/10.1016/j.jnucmat.2018.02.007

[4] S. Pace, V. Cannillo, J. Wu, D.N. Boccaccini, S. Seglem, A.R. Boccaccini: Processing glass-pyrochlore composites for nuclear waste encapsulation. *J. Nucl. Mater.* **2005**, 341, 12-18. https://doi.org/10.1016/j.jnucmat.2005.01.005

[5] M. Higashi, R. Abe, K. Sayama, H. Sugihara, Y. Abe: Improvement of Photocatalytic Activity of Titanate Pyrochlore $Y_2Ti_2O_7$ by Addition of Excess Y. *Chem. Lett.* **2005**, 34, 1122-1123. https://doi.org/10.1246/cl.2005.1122

[6] J.K. Gill, O.P. Pandey, K. Singh: Ionic conductivity, structural and thermal properties of pure and Sr^{2+} doped $Y_2Ti_2O_7$ pyrochlores for SOFC. *Solid State Sci.* **2011**, 341, 12-18. https://doi.org/10.1016/j.solidstatesciences.2011.08.025

[7] G. Sáfrán: „One-sample concept" micro-combinatory for high throughput TEM of binary films. *Ultramicroscopy* **2018**, 187, 50-55. https://doi.org/10.1016/j.ultramic.2018.01.001

[8] G. Sáfrán, P. Petrik, N. Szász, D. Olasz, N.Q. Chinh, M. Serényi: Review on High-Throughput Micro-Combinatorial Characterization of Binary and Ternary Layers towards Databases. *Materials* **2023**, 16, 3005. https://doi.org/10.3390/ma16083005

[9] W.D. Westwood, S. Maniv, P.J. Scanlon: The current-voltage characteristic of magnetron sputtering systems. *J. Appl. Phys.* **1983**, 54, 6841. https://doi.org/10.1063/1.332006

Spatial distribution of photoexcited electrons and holes in Cu_2O/Au multicomponent nanoparticles

Dávid Kovács[1,2], András Deák[1], Dániel Zámbó[1*]

[1]*Institute of Technical Physics and Materials Science, HUN-REN Centre for Energy Research, Konkoly-Thege M. út 29-33., H-1121 Budapest, Hungary*

[2] *Department of Physical Chemistry and Materials Science, Faculty of Chemical Technology and Biotechnology, Budapest University of Technology and Economics, Műegyetem rkp. 3., H-1111 Budapest, Hungary*

*daniel.zambo@ek.hun-ren.hu

Combining the ability of semiconductor nanoparticles (NPs) to produce photogenerated electrons and holes, with noble metals capable of enhancing the spatial separation of charge carriers gained tremendous attention in material science in the recent decades. Hence, countless studies have been reported focusing on the synthesis and characterization of the photophysical and photochemical properties of multicomponent semiconductor/metal NPs. Cuprous oxide (Cu_2O) is considered an outstanding candidate for the semiconductor component, owing to its outstanding properties including its high charge carrier concentration, large exciton binding energy, non-toxicity, and its band gap being active in the visible and near UV range.[1–3] In spite of the excessive research of multicomponent NPs, to reveal insight into the photogenerated charge carriers' spatial distribution as well as its influence on the photophysical and photochemical properties in Cu_2O/Au multicomponent NPs with well-controlled morphology remained unexplored. In this paper, wet-chemical syntheses were elaborated to realize pristine Cu_2O NPs (Figure 1a-c) as well as their heterostructured counterparts containing Au in two different arrangements: (i) individual gold nanorods (AuNRs) were embedded inside the Cu_2O NPs' center (Figure 1d-f), and (ii) gold nanograins (AuNGs) were grown onto the surface of the Cu_2O NPs with the same atomic quantity (Figure 1g-i). All of the three NP systems possessed octahedral shape with ca. 140 nm base edge length and identical Cu_2O content. The high morphological control enabled to reveal, how the presence and position of the Au affect the photo-physicochemical properties of the pristine Cu_2O nanooctahedra.[4]

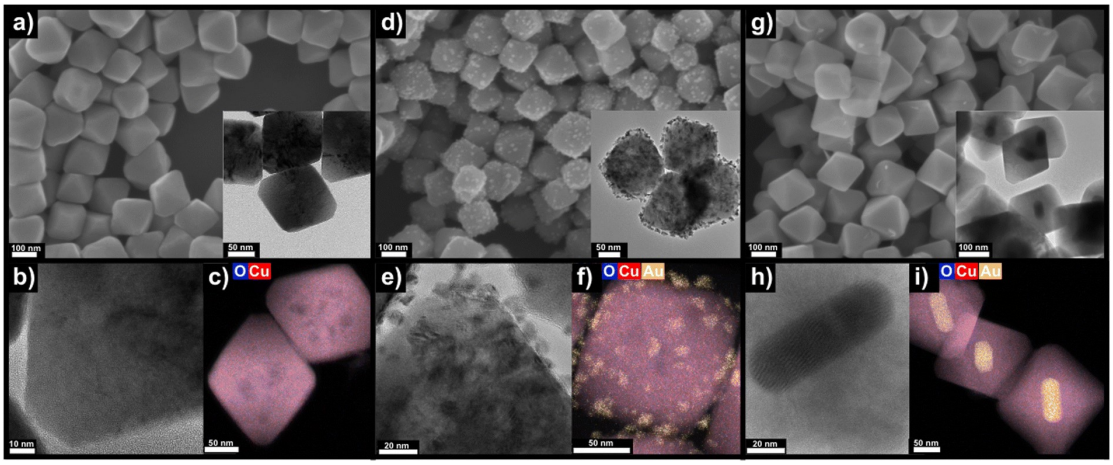

Figure 1. *Representative SEM images of the nanoparticles with high magnification TEM images in the insets, as well as atomic-resolution TEM images and elemental distribution EDS maps for the pristine (a-c), the AuNG-decorated (d-f), and the AuNR-embedded Cu_2O nanooctahedra (g-i), respectively.*[4]

The octahedral-shaped Cu_2O enclosed with 〈111〉 facets has been found to possess the highest catalytic performance among the different morphologies.[1] However, the restrained mobility of the photoexcited charge carriers associated with the vast defect states of metal-oxide semiconductors limits their potential in catalytic applications. Direct contact with noble metals provides a platform to overcome this limitation by separating the photoexcited electrons and holes. The aim of the study was to untangle the distribution of the charge carriers photoexcited in the semiconductor compartment of the NPs. To exclude the presence of hot electrons originating from the plasmonic nature of Au, a low-energy UV flashlight with a wavelength of around 400 nm served as an excitation source, that is off-resonant with the plasmon resonance of Au. In this case, the dominant charge carrier generation process is addressed to the band-to-band transition in Cu_2O.

To shed light on the nanoparticles' optical properties, absorption and excitation spectra in the UV-Vis-NIR region as well as photoluminescence (PL) spectra and time-correlated single photon counting (TCSPC) were recorded at 0.5 mM Cu_2O concentration for each of the three nanoparticle model systems (Figure 2). For the multicomponent NPs, both the decrease of the PL intensity and the faster decay of the fluorescence lifetime indicate an enhanced charge carrier separation compared to that of the pristine Cu_2O.

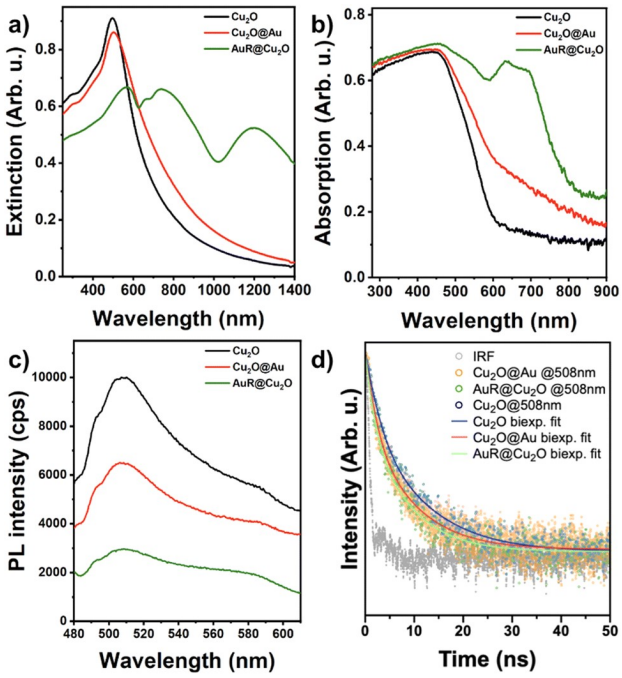

Figure 2. *Extinction (a), absorption (b), and PL (c) spectra as well as TCSPC (d) of the multicomponent NP model systems at 0.5 mM Cu_2O concentration for each measurement.*[4]

From the absorption spectra of the pristine Cu_2O NPs, the band gap energy was determined by the Tauc-plot and resulted to be 2.15 eV, which is in-line with the reported band-gap.[1] Additionally, the relative work functions were determined by single-point Kelvin probe: relative to the pristine Cu_2O nanooctahedra, –150 meV and +145 meV contact potential differences were measured for the AuNG decorated and for the AuNR-embedded Cu_2O nanooctahedra, respectively. Comparing the valence band maxima (determined by XPS) of the different Au/Cu_2O NPs, 430 meV larger binding energy was measured for the AuNR-embedded particles, indicating a higher valence band maximum for the AuNG decorated model system. The work function of the 〈111〉 facets of Cu_2O was experimentally determined by *Tan et al* (4.80 eV).[5] Previous studies showed, that the work function of Au NPs shows a size-dependent nature in the 3-10 nm size regime, attributed to their electrostatic interaction with the adjacent materials: upon decreasing the size of the Au particle, its Fermi level changes from 5.3 eV (bulk Au) to 3.6 – 3.8 eV (7 nm Au grain on Si/SiO_2 surface).[6] Based on the above considerations, the energy landscape was proposed (Figure 3). In the case of the AuNG decorated model system, the work function decreases at the Cu_2O/Au interface, resulting in a downward band bending upon the equilibration of the Fermi levels. Consequently, a Schottky barrier forms for the holes, thus, the electrons and holes are accumulated in the AuNGs and the Cu_2O surface, respectively. In contrast, the equilibration of the Fermi levels in the AuNR-embedded model system results in an upward band bending, resulting in a Schottky barrier for the electrons. Consequently,

the electrons and holes are accumulated in the Cu_2O and the AuNR, respectively. This implies a fundamentally different charge separation process in the engineered multicomponent particles dictating the avalability of the electrons and holes in a photocatalytic reaction.

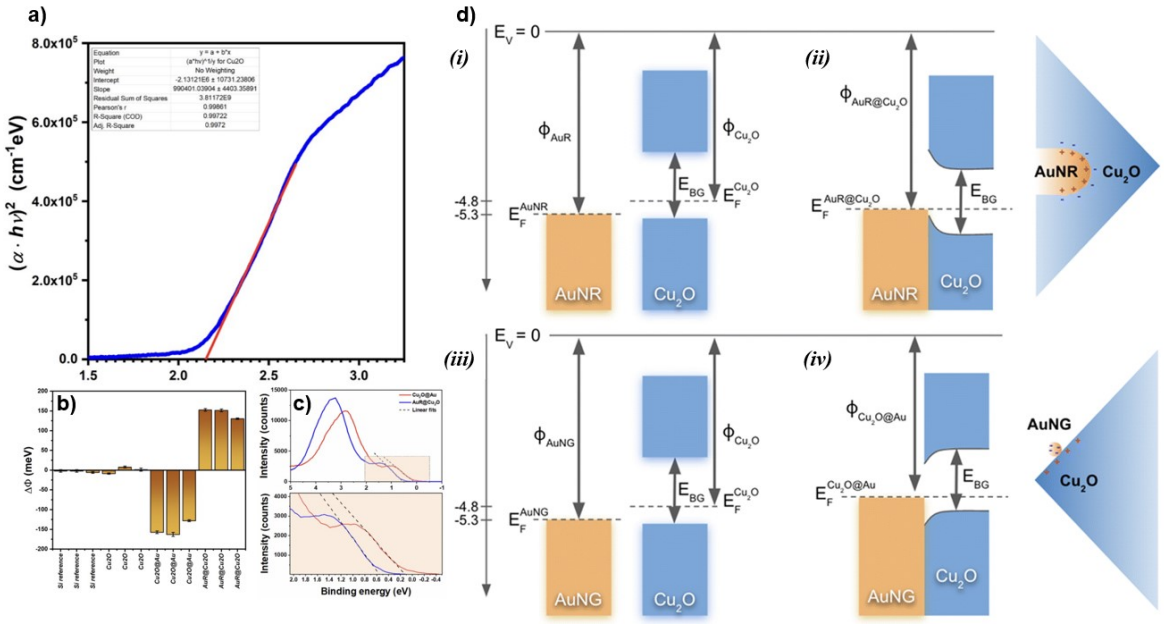

Figure 3. *Tauc plot of the pristine Cu_2O NPs served to determine the bad gap energy (a). Determination of the contact potential differences by single-point Kelvin probe (b). Valence band spectra of the multicomponent NPs measured by XPS (c). Schematic energy landscape diagram comparing the AuNR-embedded (i and ii) and the AuNG-decorated (iii and iv) multicomponent NPs before and after the contact, respectively.*[4]

This hypothesis was also tested in the photocatalytic degradation reaction of methyl orange. Decoration of the Cu_2O nanooctahedra with small Au nanograins enabled enhanced activity and resistance against photocorrosion compared to the AuR/Cu_2O and pristine Cu_2O NPs.

In conclusion, it can be declared that the presence of gold in Cu_2O nanooctahedra significantly improves the photocatalytic activity, and provides a platform to utilize a low-power UV illumination, in which condition the pristine Cu_2O nanooctahedra is inactive. Furthermore, it has been shown that besides the presence, the position of gold is also crucial from the application point of view. The morphological arrangement of the nanograin-decorated model system provides the simultaneous availability of both charge carriers, favoring the photocatalytic performance as well as the photostability of the nanoparticles.

Acknowledgments

D. K. acknowledges the support of Pro Progressio and József Varga Foundation. Project no. TKP2021-NKTA-05 has been implemented with the support provided by the Ministry of Innovation and Technology of Hungary from the National Research, Development and Innovation Fund (NRDI), financed under the TKP2021 funding scheme. Moreover, the work was supported by the NRDI Fund of Hungary under the grant of FK 142148.

References

(1) Huang, M. H. Facet-Dependent Optical Properties of Semiconductor Nanocrystals. *Small* **2019**, *15* (7), 1804726. https://doi.org/10.1002/smll.201804726.

(2) Sun, S.; Zhang, X.; Yang, Q.; Liang, S.; Zhang, X.; Yang, Z. Cuprous Oxide (Cu2O) Crystals with Tailored Architectures: A Comprehensive Review on Synthesis, Fundamental Properties, Functional Modifications and Applications. *Progress in Materials Science* **2018**, *96*, 111–173. https://doi.org/10.1016/j.pmatsci.2018.03.006.

(3) Steinhauer, S.; Versteegh, M. A. M.; Gyger, S.; Elshaari, A. W.; Kunert, B.; Mysyrowicz, A.; Zwiller, V. Rydberg Excitons in Cu2O Microcrystals Grown on a Silicon Platform. *Commun Mater* **2020**, *1* (1), 1–7. https://doi.org/10.1038/s43246-020-0013-6.

(4) Kovács, D.; Deák, A.; Radnóczi, G. Z.; Horváth, Z. E.; Sulyok, A.; Schiller, R.; Czömpöly, O.; Zámbó, D. Position of Gold Dictates the Photophysical and Photocatalytic Properties of Cu2O in Cu2O/Au Multicomponent Nanoparticles. *J. Mater. Chem. C* **2023**, *11* (26), 8796–8807. https://doi.org/10.1039/D3TC01213A.

(5) Tan, C.-S.; Hsu, S.-C.; Ke, W.-H.; Chen, L.-J.; Huang, M. H. Facet-Dependent Electrical Conductivity Properties of Cu2O Crystals. *Nano Lett.* **2015**, *15* (3), 2155–2160. https://doi.org/10.1021/acs.nanolett.5b00150.

(6) Zhang, Y.; Pluchery, O.; Caillard, L.; Lamic-Humblot, A.-F.; Casale, S.; Chabal, Y. J.; Salmeron, M. Sensing the Charge State of Single Gold Nanoparticles via Work Function Measurements. *Nano Lett.* **2015**, *15* (1), 51–55. https://doi.org/10.1021/nl503782s.

On the inevitable role of shape in engineering porous multimetallic nanoparticles for catalytic applications

Apoko S. Omondi[1,2], Dávid Kovács[1,2], András Deák[1] and Dániel Zámbó[1*]

[1]*Institute of Technical Physics and Materials Science, HUN-REN Centre for Energy Research, Konkoly-Thege M. út 29-33., H-1121 Budapest, Hungary*

[2] *Department of Physical Chemistry and Materials Science, Faculty of Chemical Technology and Biotechnology, Budapest University of Technology and Economics, Műegyetem rkp. 3., H-1111 Budapest, Hungary*

*daniel.zambo@ek.hun-ren.hu

Structural, compositional, and surface chemical diversity of well-designed metal nanoparticles catalyzed a rapid expansion of their application potential in the recent decade. Recently, wet-chemical synthetic methods have been improved significantly, thus, the morphology of the nanoparticles can be varied as well as controlled ensuring the preparation of high-quality, monodisperse particles having even exotic shapes. It has been demonstrated that noble metals, especially Au, Pd, Pt, Ir and Ru, are promising heterogeneous and electrocatalysts both in reduction and oxidation reactions. Although performing catalysis using non-noble metal elements has been in the spotlight of the research, the intrinsic activity of platinum in hydrogen evolution reaction (HER) as well as in ethanol oxidation reaction (EOR) highly exceeds that of the earth-abundant catalysts.[1,2] Numerous studies aimed for untangling the shape/property correlation of mono- and bimetallic nanoparticles in catalysis,[3,4] while precisely controlled multimetallic colloids are much less investigated. The reasons for this might root in the challenging synthetic procedures, the lack of compositional control at the nanoscale restricting the exploration of the above-mentioned correlation. Multielemental synergy at the nanoscale is a tool for amplifying the advantageous properties (optical, electronic, etc.) of the components being in the close vicinity of each other, which can be logically ensured in a form of a nanoparticle.

Utilization of multimetallic, noble metal-based nanoparticle catalysts requires the consideration of various properties affecting the catalytic activity. The position of the d-band in each metal component is of great importance in the overall electronic properties of a multicomponent particle. This governs the intermetallic charge transport and the strength of the bonds of the adsorbates and intermediates. Combining Au with Pd (or Pd with Pt) not solely significantly lowers the d-band position of Pd (or Pt) manifesting in weaker chemisorption of poisonous intermediates, but also increases the long-term stability and durability of the catalysts.[5] Moreover, the oxophilicity controls the coverage of the adsorbed O species (O_{ad}): Pd is more oxophilic than Pt which supports lowering the overpotential in EOR.[6] Additionally, incorporating Ir into the picture further contributes to increase the CO tolerance and C-C cleavage. It is known that most of the electrooxidation reactions are structure-sensitive which requires the proper shape control of the nanocatalyst and prioritize core/shell structures over alloys.[7] Obviously, surface area, mass transport and electron

transfer processes are closely connected highlighting the essential importance of availability of the active sites, hence, the surface area.

Surface area in case of nanoparticles can be increased either by decreasing the particle size or preparing porous structures. Ideally, this can be achieved by designing the multimetallic catalysts being intrinsically porous and consisting of small sub-building blocks at the same time. The main approach involves using micellar templates during the synthesis, which are removed post-synthetically. Triblock copolymers are promising candidates for this purpose due to their size-tunability and compatibility with the reaction conditions. Performing particle synthesis in the presence of polymer micelles aids the deposition of the metals directed into the regions not occupied by the micellar template. This results in the formation of mesopores improving the availability of active sites and drastically increasing the surface area.[8,9]

As a prototypical gold nanoparticle morphology, gold nanorods (AuNRs) are frequently used as catalyst or core particle due to their plasmonic properties. We also chose AuNRs as a 'support particle' to prepare tetrametallic nanorods by depositing Pd, Pt and Ir in a form of a shell around the AuNRs.[8] Due to the shell formation, the longitudinal dipolar resonance of the nanorods is significantly damped and the particles absorb in the UV-Vis-NIR wavelength region (Figure 1a).

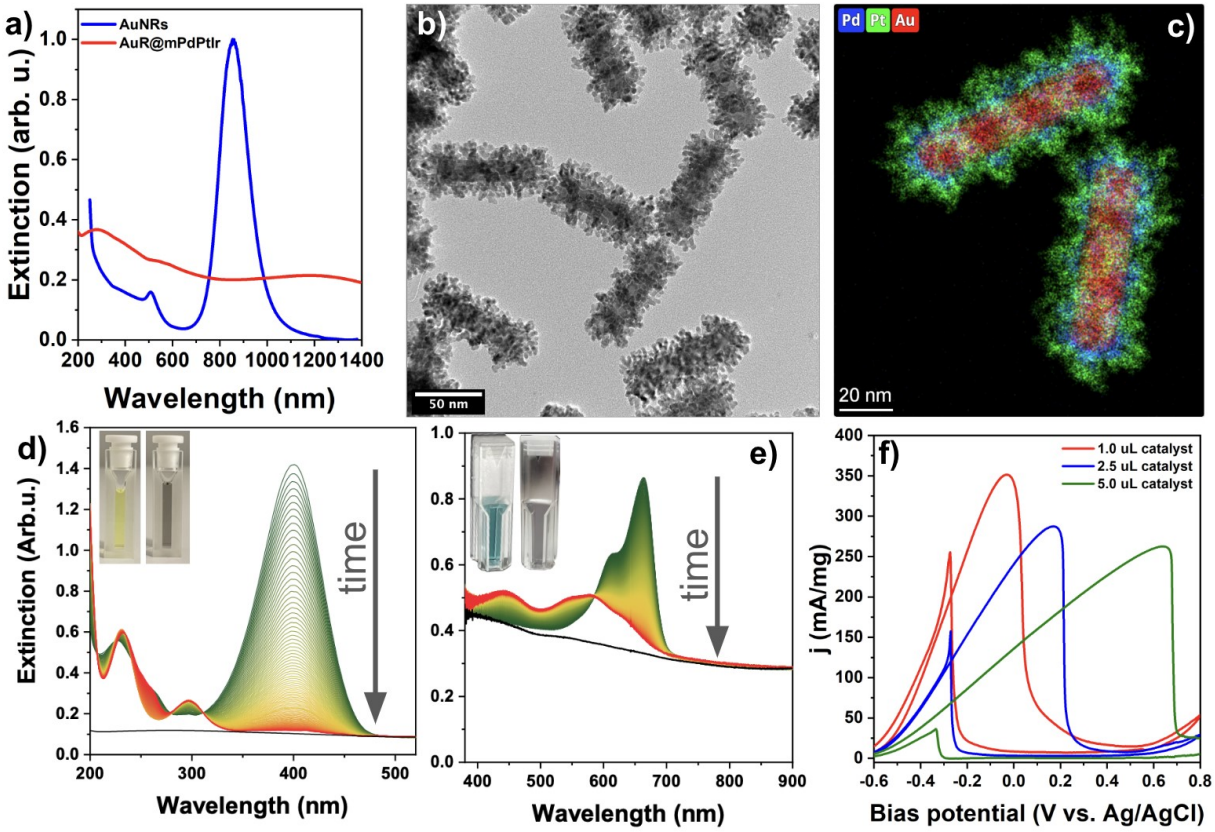

Figure 1. *Extinction spectrum of the Au nanorods and the tetrametallic nanorods (a), structure (b) and elemental composition (c) of Au@PdPtIt tetrametallic nanorods. Time-resolved spectra during the catalytic reaction of p-nitrophenol (d) and methylene blue (e). Electrooxidation of ethanol (f). Adapted from Ref. 8.*

The shell of the monodisperse tetrametallic particles shows high micro- and mesoporosity (Figure 1b) and contains the metals in a layered form (Figure 1c). The particles were tested in three catalytic

model reactions: (i) conversion of p-nitrophenol to p-aminophenol (Figure 1d), (ii) N-demethylation of methylene blue dye (Figure 1e), and (iii) ethanol electrooxidation reaction (Figure 1f).[8]

While the first two reactions occur in solution (namely catalyzed by dispersed colloidal particles) and can be monitored in time by spectroscopy, EOR is a heterogeneous electrocatalytic process required the fabrication of a working electrode by depositing the multimetallic nanorods on ITO substrate. All reactions take place at ambient conditions without external trigger (*e.g.* heat, light) and the particles were found to be robust, recyclable without changing their original morphology.[8] For EOR, the effect of the catalyst loading on the mass activity was also tested: the lower the loading the higher the mass activity and the low loading (equals to 74 $\mu g/cm^2$) enables to perform the reaction at low overpotential (Figure 1f).

The efficiency and performance of the rod-shaped tetrametallic particles inspired the extension of the research by investigating the effect of the core particle's morphology on the catalytic activity.[9] It is known that the optical, electronic, and catalytic properties of noble metal particles strongly depend on their size and shape. The aim was to compare the heterogenous and electrocatalytic performance of the multimetallic particles which have identical surface chemistry, elemental composition and core particle's volume but their morphology significantly differs: isometric gold nanospheres and symmetry-broken shapes (nanorod, nanoprism, nanooctahedron and nanobipyramid) were synthesized and used to carry the trimetallic porous shell.

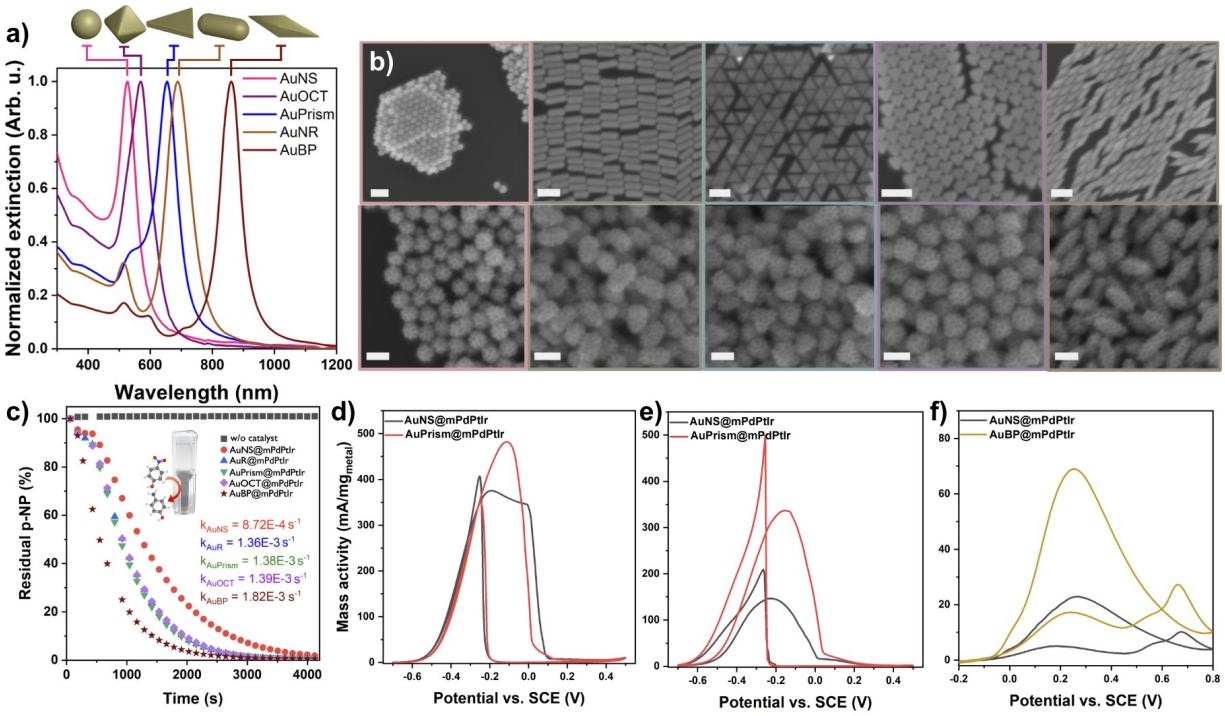

Figure 2. *Extinction spectra of the gold core particles with different morphologies (a). SEM images of the cores and core/shell particles color coded the same way as in the spectra (b). Time-dependent p-nitrophenol reduction and the corresponding rate constants (c). Best and worst performing particle shapes in MOR (d), EOR (e) and FAOR (f). Adapted from Ref. 9.*

For this comparison, the key requirement is to prepare high-quality and monodisperse particle to avoid the distorting effect of any biproducts. Figure 2a shows the extinction spectra of the Au core particles clearly demonstrating their outstanding shape purity. SEM images of the core and core/shell

particles prove their excellent quality and the porous nature of the tetrametallic particles (Figure 2b).[9] Since the particle solutions were prepared in a way that their total metal concentrations were set identical, the shape-dependent catalyic performance could be tested in p-nitrophenol reduction and methanol/ethanol/formic acid electrooxidation. All test reactions were carried out at ambient temperature and pressure without the use of external trigger (heat, light). Temporal monitoring the degradation of p-nitrophenol revealed the inevitable role of the morphology on the catalytic reaction rate: while spherical particles converts the p-NP the slowest, symmetry-broken particles show higher activity, especially the bipyramidal morphology surpasses the others (Figure 2c). While similar (but not the same) trend can be seen in electrooxidation reactions, different particle shapes perform differently in MOR, EOR and FAOR. In MOR and EOR (Figure 2d,e), tetrametallic nanoprisms were found to be superior. The mass transport limitations can also be lowered by using nanoprisms in MOR (Figure 2d). Interestingly, the best performing electrocatalyts in formic acid oxidation are the tetremetallic bipyramids (Figure 2f), however, the prisms perform also well.[9]

There might be different processes and properties governing the shape-dependent activity. It is important, however, that the multimetallic shell formation endows the particles with highly negative surface charge, which can be attributed to the intraparticle charge transport upon equilibration of the Fermi levels of the different metals. Nevertheless, different surface facets also play an important role in the resistancy of the catalyst against CO poisoning. Moreover, the enhanced surface area of the porous particles is of central importance. To determine the surface area differences, the electrocatalyitically active surface area (ECSA) of the tetrametallic nanoparticles with different morphologies was calculated based on the double layer capacitances (Figure 3a) measured electrochemichemically.

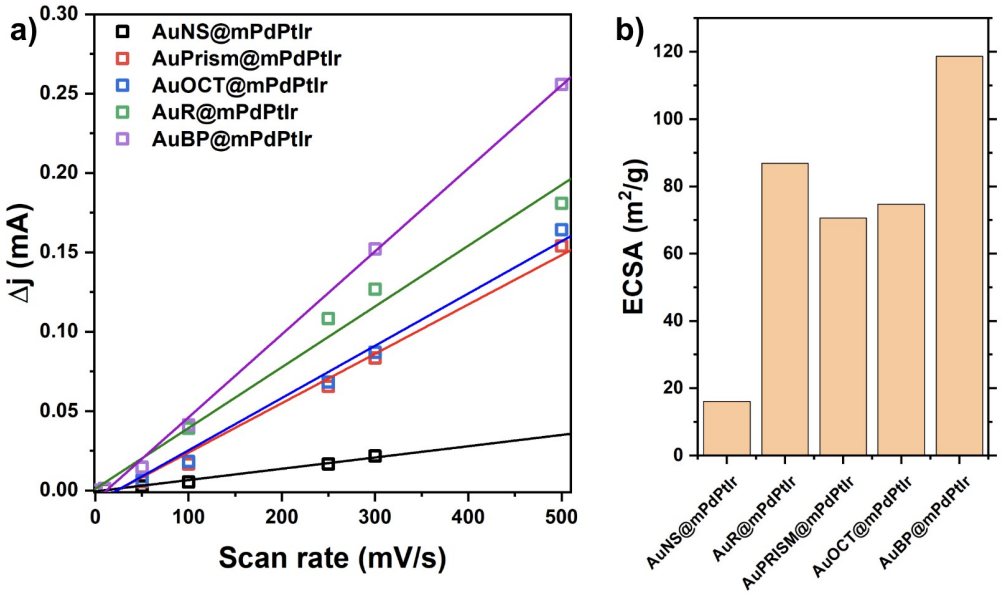

Figure 3. *Electrochemical measurements for determining the double layer capacitance of the particles with different shapes (a). Calculated ECSA values for the tetrametallic nanoparticles (b). Adapted from Ref. 9.*

It was found that the nanospheres have the lowest ECSA, while nanorods and bipyramids show the highest surface area (Figure 3b). Considering the fact that the nanoprims perform well in electrooxidation reaction, the ECSA itself does not explain the correation between the morphology and catalytic activity. This underlines the importance of preparing properly designed nanoparticles

with tailored shape for the specific, desired application. Nonetheless, symmetry-breaking is a perfect tool to enhance the activity of the noble metal nanocatalysts.[9]

Keywords: multimetallic nanocatalyst, symmetry-breaking, electrocatalysis, heterogeneous catalysis

References

(1) Hansen, J. N.; Prats, H.; Toudahl, K. K.; Mørch Secher, N.; Chan, K.; Kibsgaard, J.; Chorkendorff, I. Is There Anything Better than Pt for HER? *ACS Energy Lett.* **2021**, *6* (4), 1175–1180. https://doi.org/10.1021/acsenergylett.1c00246.

(2) Rizo, R.; Pérez-Rodríguez, S.; García, G. Well-Defined Platinum Surfaces for the Ethanol Oxidation Reaction. *ChemElectroChem* **2019**, *6* (18), 4725–4738. https://doi.org/10.1002/celc.201900600.

(3) Zhang, J.; Wan, L.; Liu, L.; Deng, Y.; Zhong, C.; Hu, W. PdPt Bimetallic Nanoparticles Enabled by Shape Control with Halide Ions and Their Enhanced Catalytic Activities. *Nanoscale* **2016**, *8* (7), 3962–3972. https://doi.org/10.1039/C5NR05971B.

(4) Li, G.; Zhang, W.; Luo, N.; Xue, Z.; Hu, Q.; Zeng, W.; Xu, J. Bimetallic Nanocrystals: Structure, Controllable Synthesis and Applications in Catalysis, Energy and Sensing. *Nanomaterials* **2021**, *11* (8), 1926. https://doi.org/10.3390/nano11081926.

(5) Hammer, B.; Nørskov, J. K. Theoretical Surface Science and Catalysis—Calculations and Concepts. In *Advances in Catalysis*; Elsevier, 2000; Vol. 45, pp 71–129. https://doi.org/10.1016/S0360-0564(02)45013-4.

(6) Santos, R. M. I. S.; Nakazato, R. Z.; Ciapina, E. G. The Dual Role of the Surface Oxophilicity in the Electro-Oxidation of Ethanol on Nanostructured Pd/C in Alkaline Media. *Journal of Electroanalytical Chemistry* **2021**, *894*, 115342. https://doi.org/10.1016/j.jelechem.2021.115342.

(7) Kang, S. W.; Lee, Y. W.; Park, Y.; Choi, B.-S.; Hong, J. W.; Park, K.-H.; Han, S. W. One-Pot Synthesis of Trimetallic Au@PdPt Core–Shell Nanoparticles with High Catalytic Performance. *ACS Nano* **2013**, *7* (9), 7945–7955. https://doi.org/10.1021/nn403027j.

(8) Zámbó, D.; Kovács, D.; Radnóczi, György Z.; Horváth, Z. E.; Sulyok, A.; Tolnai, I.; Deák, A. Structural Control Enables Catalytic and Electrocatalytic Activity of Porous Tetrametallic Nanorods. *Small* **2024**, *20* (31), 2400421. https://doi.org/10.1002/smll.202400421.

(9) Omondi, A. S.; Kovács, D.; Radnóczi, G. Z.; Horváth, Z. E.; Tolnai, I.; Deák, A.; Zámbó, D. Symmetry Breaking Enhances the Catalytic and Electrocatalytic Performance of Core/Shell Tetrametallic Porous Nanoparticles. *Nanoscale* **2024**, 10.1039.D4NR03589E. https://doi.org/10.1039/D4NR03589E.

Optical calibration of the ellipsometric mapping tool from cheap parts

Berhane Nugusse[1,2], György Juhász[1], Csaba Major[1], Péter Petrik[1,4], Sándor Kálvin[1], Zoltán György Horváth[3], Miklós Fried[1,2*]

[1]*Institute of Technical Physics & Materials Science, Centre for Energy Research, Konkoly-Thege Rd. 29-33, Budapest 1121, Hungary*

[2]*Institute of Microelectronics and Technology & Doctoral School on Materials Sciences and Technologies, Óbuda University, Budapest, Hungary*

[3]*Institute for Solid State Physics & Optics, Wigner Research Centre for Physics, Konkoly-Thege Rd. 29-33, Budapest 1121, Hungary*

[4]*Department of Electrical Engineering, University of Debrecen, Debrecen, Hungary*

Non-destructive techniques are important methods to use during all stages of the thin film processes. Spectroscopic Ellipsometry (SE) is one of such methods.

SE is a non-destructive, noninvasive and non-intrusive optical technique. It is a technique that measures the change in polarization state of the measurement beam induced by reflection from or transmission though the sample. Ellipsometry measures the amplitude ratio (tan ψ) and phase difference (Δ) between the parallel (p) and normal (s) polarizations. During data analysis, information about the system under the study is obtained by fitting measured ellipsometric spectra to optical and structural models, as ellipsometry does not give a direct information of the sample in consideration.

The purpose of this work is to make a well calibrated prototype optical mapping tool for thin film measurements using only cheap parts such as an LCD monitor and a pinhole camera [1-3] with CMOS Sensor with Integrated 4-Directional Wire Grid Polarizer Array (Sony's IMX250MYR CMOS), shown in Fig.2. Our arrangement shows similarity to the solution of Bakker et al [4], using a computer screen as a light source and a webcam as a detector in an imaging off-null ellipsometer.

During the conventional ellipsometric mapping, the data collection is relatively slower and use a scanned small spot, while our new optical mapping tool from cheap parts measures a big area in one shot. Specifically, in this paper the special focus is on a newly developed calibration method. The thickness map result is independently cross checked using a commercial Woollam M2000 ellipsometer and the agreement is within 1 nm, which makes our optical mapping tool a good candidate for industrial purposes.

We know two industrial systems which are capable to measure big (square meter size) samples: Semilab FPT system (https://semilab.com/hu/product/799/fpt) and the Woollam AccuMap (https://www.jawoollam.com/download/pdfs/accumap-se-brochure.pdf) system. Both systems use “traditional” SE device (100 kUSD price) in special big moving/scanning system, measuring point-by-point the big samples. The Woollam brochure writes that "Data Acquisition Rate: < 6 seconds per point (includes time for movement to new point, automated alignment, and data collection)" so it can measure one big area during several 10 minutes. Our system can measure within seconds during one shot

The new concept of the non-collimated beam ellipsometer prototype is set up as shown in Fig. 1

A LED-LCD monitor (or a TV), see Fig. 1 a) (C) serves the polarized RGB colored light (aee the built-in polarizer sheet, number 4 in Fig. 1 b) and a polarization sensitive camera behind a pinhole

(7&8) together. The LCD monitor (Dell UltraSharp™ U2412M, GB-LED) is used in a 45-degree rotated position, measured by a digital angle gauge with 0.1 deg precision. In straight-through position, we can detect the extinction of the polarization sensitive camera better than 10^{-2}.

The polarization sensitive camera sensor (The Imaging Source Company's DYK 33UX250 USB 3.0 Polarsens camera), see in Fig. 1 a) (A) and in Fig. 2, serves the polarization state data, from 0, 45, 90, 135-degree rotation positions (plus 3 RGB colors in each position). This arrangement is equal to a conventional static photometric rotating analyzer ellipsometer.

The sample is illuminated by a non-collimated light through a fixed polarizer at an azimuth of 45 degrees to the plane of incidence. The reflected light passes through a virtual "rotating analyzer" and the intensity is captured by a two-dimensional position sensitive photodetector system at four different angular positions of the analyzer.

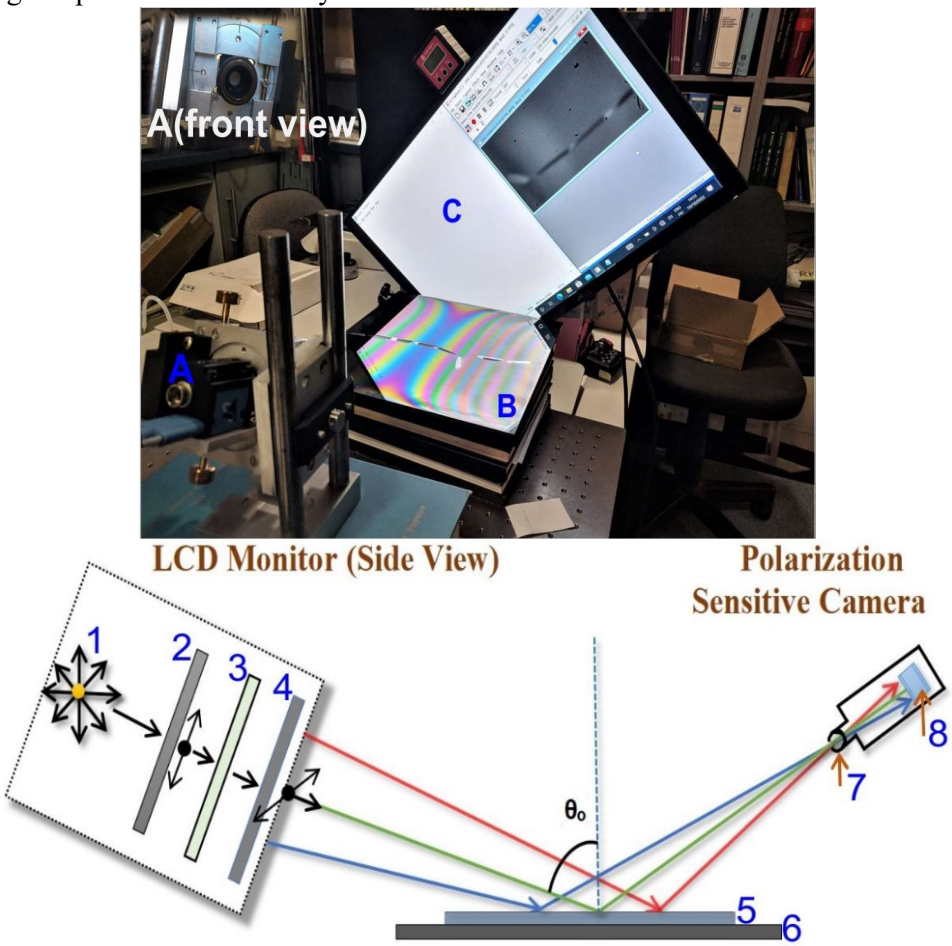

Figure 1. *(a) Experimental set-up: A) Polarization sensitive camera B) Sample + Sample holder C) LCD monitor rotated into 45° position – Upper-left: the pinhole in front of the camera (b) Schematics of the non-collimated beam ellipsometer: 1) Light source 2) Vertical polarizer 3) Liquid crystal cell 4) Horizontal polarizer - (C) 5) Sample - (B) 6) Sample holder 7) Pinhole (sub-mm size) 8) Camera sensor (A)*

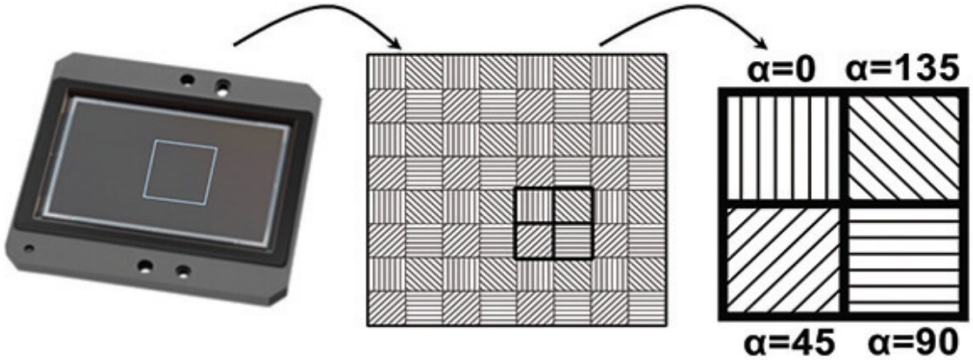

Figure 2. *Schematic structure of a 2/3 inch Sony CMOS Pregius Polarsens sensor (IMX250MZR) a). Camera sensor b). Polarizer array matched to detector pixels c). Unit cell (Super pixel)*

Minimum 3 different analyzer positions are required. These four polarization states (intensity) data (at 0, 45, 90, 135-degree rotation positions) are enough (the fourth date is good to reduce the error) to determine the ellipsometric angles: ψ and Δ. Our camera serves the data for 3 colors, so we have 3x2 measured ψ and Δ.

Schematic structure of a 2/3-inch Sony CMOS Pregius Polarsens sensor (IMX250MZR) is shown in Fig. 2 b) and c). The main advantage of the assembly is that no moving parts in the system!).

It is a common scientific practice to check any device or a setup for an accuracy and precision and trying to correct any errors or malfunctions on the setup through calibration and comparing with other corresponding standard models. Accordingly, a direct monitor measurement is taken in our setup and we noticed, rather confirmed, that we need error correction and calibration of the experiment setup.

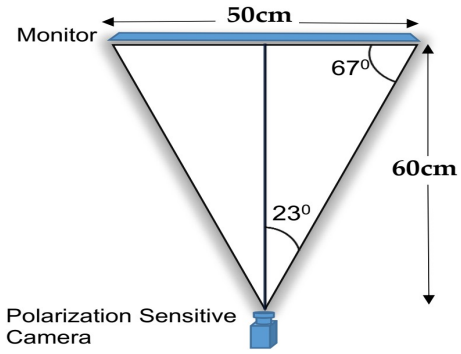

Figure 3. *Schematic drawing of the direct ellipsometric measurement of monitor.*

Theoretically, perfect linearly polarized light is coming from the monitor at 3 different (red, green, blue) light-bands. We directed the camera to the monitor performing a direct ellipsometric measurement without a sample, see Fig. 3. If we have an ideal sample which do not change the polarization state then we measure tan ψ and cos Δ values to 1 in each point. This measurement shows the fact that a point-by-point ρ-correction calibration is needed.

Figure 4 shows the result of direct-monitor measurements, tan ψ and cos Δ values for each color, Red, Blue and Green. The systematic alterations from 1 in the maps show systemat-ic measurement errors in our optical mapping tool that justify the need for a special calibration.

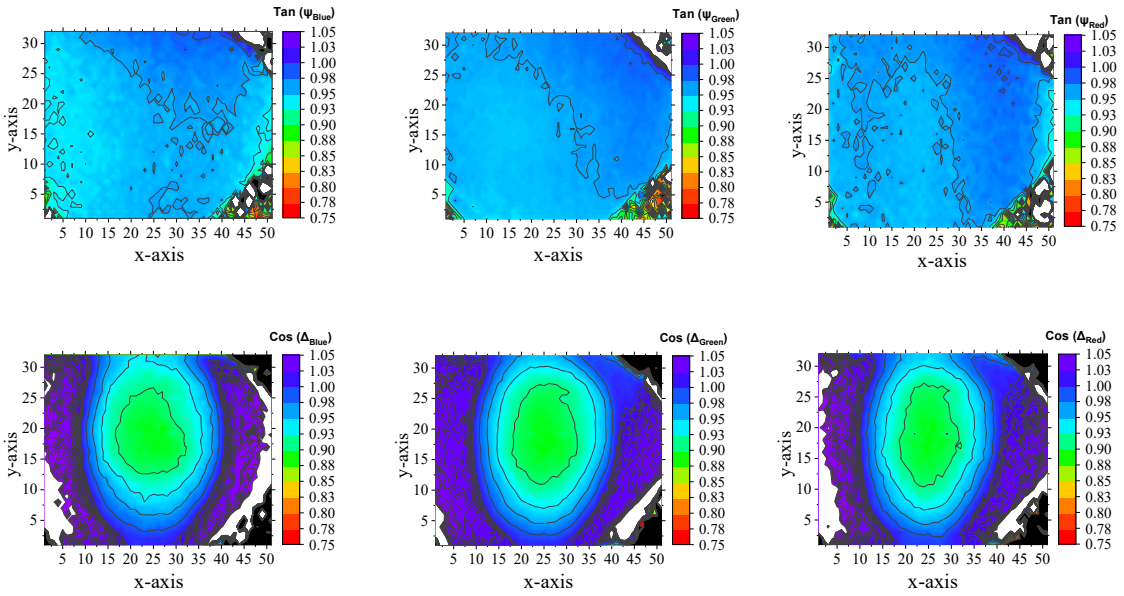

Figure 4. *3D Experimental results of tan ψ and cos Δ values for each color from the direct monitor measurement. Note that, the x and y-axes our figures represent the pixel group in the sample, 51x32 and the z-axis (color band) shows the range of the measurement values in each corresponding category, depending on the type of the map.*

Three SiO_2/Si samples of nominally 40, 60 and 100 nm thickness were used for the calibration process and another nominally 80 nm SiO_2/Si sample was analyzed using the calibration values from the three oxide samples. The experimental data is collected for each three oxide samples and then, six different positions of each sample was used in the calibration process. The experimental figures shown in this paper are mostly deduced by excluding pixels with high MSE values that deviate the results from the true expected values, prioritizing points of only low MSE. Figure 5 (b) shows the MSE-map of the central 20x15 cm part where the measurement proved to be reliable.

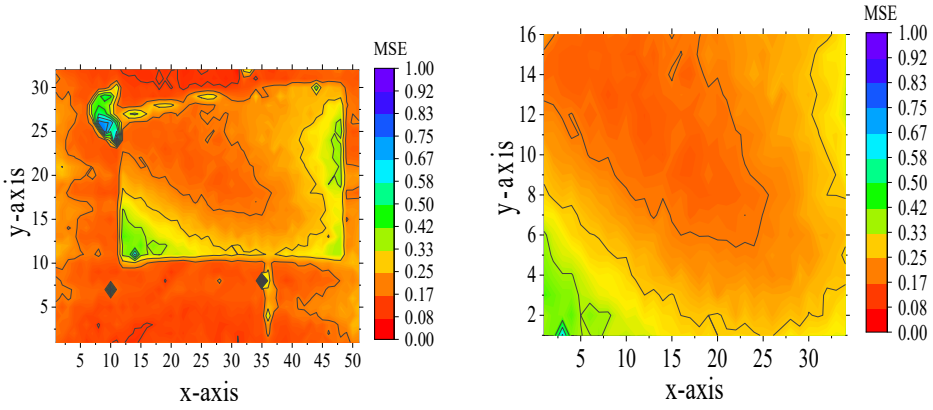

Figure 5. *(a). Merged MSE full map (b). Low MSE pixels map*

Monitor-correction are calculated using the following equation:

$\rho_{opt}=\rho_{meas}*\rho_{monitor}$ *(different for each point and each wavelength)*

where ρ_{opt} is the measured value with perfect light source, ρ_{meas} is the actually measured value and $\rho_{monitor}$ is the ρ-correction. We measure three SiO_2/Si samples with different thicknesses. We determine 3*N*2 ψ and Δ (where N is the number of different wavelengths, presently 3) and we should calculate (fit) 2*N+3+1 unknown calibration values for a full calibration: N*real ($\rho_{monitor}$) and N*im($\rho_{monitor}$) + 3 thicknesses + 1 actual angle of incidence in each points and each wavelengths. Each thickness and angle-of-incidence in the sample depends only on location, but the ρ-corrections ($\rho_{monitor}$) are location and wavelength dependents. This implies ρ-corrections give more insight on the nature and status of the sample measurement.

The result of the angle-of-incidence calibration is shown in Figure 6. Using the same criterions (low MSE, smooth map), we refined the angle-of-incidence map (Fig. 8 b) from the angle-of-incidence full map (Fig. 8 a). As it can be seen in Figure 8 (b), the angle-of-incidence varies smoothly across the surface, which agrees with the theoretical values. This refined angle-of-incidence map was used later to evaluate the nominally 80 nm SiO_2/Si sample thickness map.

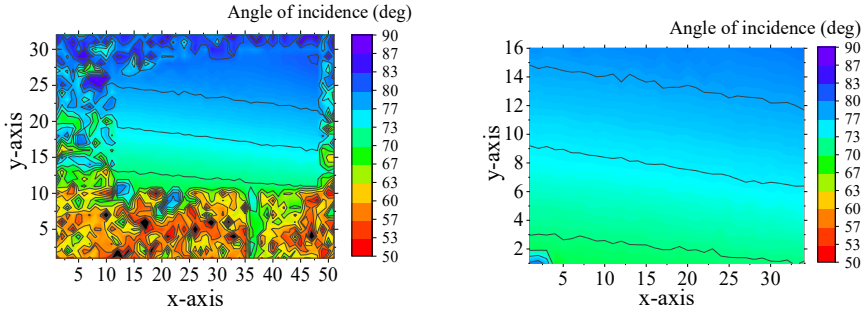

(a) *b)*

Figure 6. *a). Angle of incidence full map b). Angle of incidence with high MSE pixels removed*

The same calibration process resulted the thickness maps of our calibration oxide samples (nominally 40, 60 and 100 nm thickness) which are shown in Figure 7.

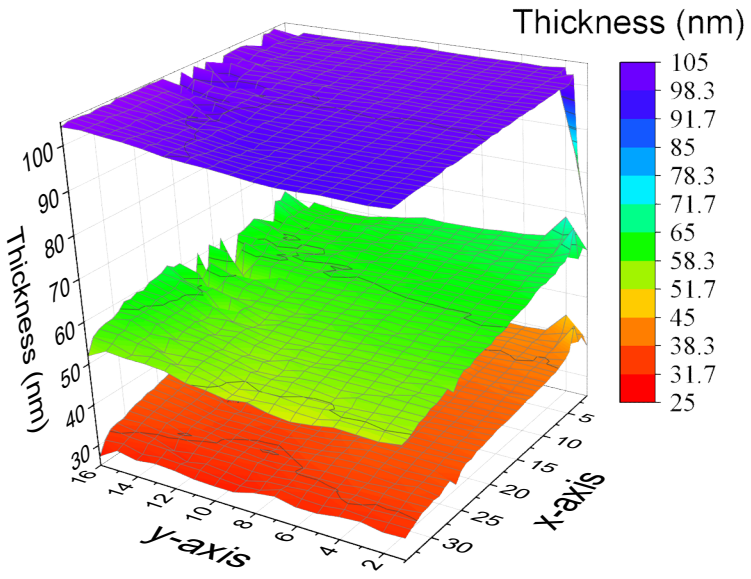

Figure 7. *Thickness maps of nominally 40 nm, 60 nm and 100 nm of SiO_2/Si samples (low MSE areas) from the refined central 20x15 cm part.*

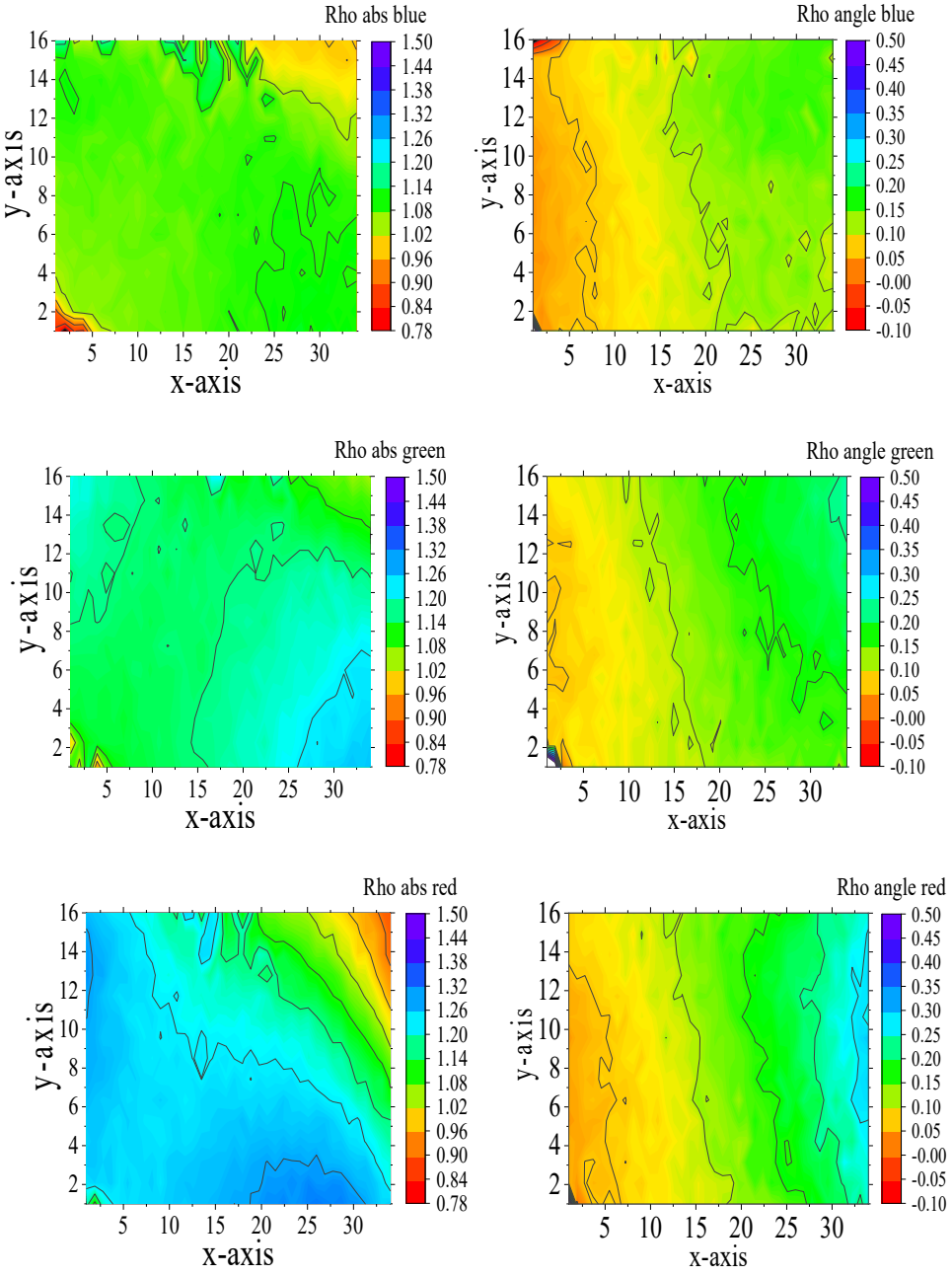

Figure 8. *The calibrated $\rho_{monitor}$ values. Left column: real ρmonitor, rigth column: phase shift-correction in rad. Upper row: blue (450 nm), Middle row: green (550 nm), Lower row: red (650 nm)*

The calibrated $\rho_{monitor}$ values for the specific setting of the device are also mapped, see Figure 8. These values differ only by less than 0.3 from the ideal values, so we can use them to evaluate independent measurements.

We used a nominally 80 nm thick, 20 cm diameter SiO_2/Si sample to check the results of the calibration. We used the calibrated $\rho_{monitor}$ values to correct the measured ellipsometric angles and used the corrected values to determine the thickness map. The thickness map of the 80 nm oxide sample in Figure 9 (b) appears to be smooth enough. Note, that one color in Figure 9 is only 0.5 nm.

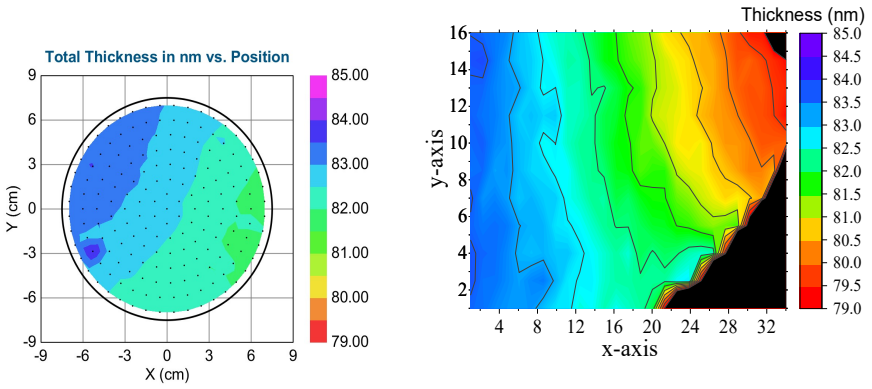

(a) (b)

Figure 9. *(a) Nominally 80 nm oxide sample thickness map by Wollam M2000 SE (Note, that our M2000 can map only the central 14 cm diameter area of the 20 cm diameter sample (b) Thickness map of same SiO2/Si sample 20x15 cm area by the non-collimated, calibrated mapping tool.*

An independent checking measurement of the same sample was also made by the Wollam M2000 ellipsometer, as shown in the Figure 9 (a). The agreement of the thickness measurement made between our non-collimated ellipsometer after correction, and the conventional Wollam M2000 ellipsometer is only within 1 nm, which is a good agreement.

Acknowledgement:

Support of Hungarian Sci.Research Fund VOC-DETECT M-era-Net project, OTKA NNE 131269 is acknowledged.

References:

[1] C. Major, G. Juhasz, Z. Labadi, M. Fried, "High speed spectroscopic ellipsometry technique for on-line monitoring in large area thin layer production," 2015 IEEE 42nd Photovoltaic Specialist Conference (PVSC), 2015, pp. 1-6, doi: 10.1109/PVSC.2015.7355640

[2] G. Juhász, Z. Horváth, C. Major, P. Petrik, O. Polgár, M. Fried, Non-collimated beam ellipsometry, physica status solidi c Volume 5, Issue 5 p. 1081-1084, https://doi.org/10.1002/pssc.200777862

[3] Horváth Z Gy, Juhász G, Fried M, Major C, Petrik P: Imaging optical inspection device with a pinhole camera; EP2160591B1, Submission Number: PCT/HU2008/000058, NSZO: G01N21/8422, Country of patent: Europe

[4] J. W. P. Bakker, H. Arwin, I. Lundström, and D. Filippini: Computer screen photoassisted off-null ellipsometry, Applied Optics Vol. 45, Issue 30, pp. 7795-7799 (2006) https://doi.org/10.1364/AO.45.007795

[5] Zereay, Berhane N. ; Kálvin, Sándor ; Juhász, György ; Major, Csaba ; Petrik, Péter ; Horváth, Zoltán G. ; Fried, Miklós: Optical Calibration of a Multi-Color Ellipsometric Mapping Tool Fabricated Using Cheap Parts, PHOTONICS 11 : 11 Paper: 1036 , 11 p. (2024) https://doi.org/10.3390/photonics11111036

Determination of solid-liquid adhesion work in a direct and absolute manner by the Capillary Bridge Probe

N. Nagy

Institute of Technical Physics and Materials Science, HUN-REN Centre for Energy Research, Konkoly-Thege M. út 29-33., H-1121 Budapest, Hungary

The need of the determination of solid-liquid adhesion work is as old as Dupré's definition of the reversible work of adhesion. In addition to its scientific importance, this quantity is a critical factor affecting product quality and performance in many industrial fields. In general, it plays crucial role if the liquid should completely cover a solid surface (e.g. coatings, paints, inks, lubricants, adhesives, pesticides) or, on the contrary, the liquid should not remain on the surface at all (liquid repellency, anti-icing, etc.).

According to Dupré's definition, the adhesion work is the reversible thermodynamic work required to separate unit area of two phases in contact. Applying this definition to solid and liquid phases, the solid-liquid adhesion work (W_a) can be written as

$$W_a \equiv \gamma_{LV} - (\gamma_{SL} - \gamma_{SV}) \tag{1}$$

where γ_{LV} is liquid's surface tension, γ_{SL} is solid-liquid interfacial tension, and γ_{SV} is the surface free energy of the solid. The last two quantities cannot be measured directly. However, their difference is included in the Young equation, which describes the condition for equilibrium of the contact line at the solid-liquid-vapor interface:

$$\gamma_{SV} - \gamma_{SL} - \gamma_{LV} \cdot \cos\vartheta = 0 \tag{2}$$

where ϑ is the contact angle at the contact line. The combination of these two equations eliminates the unknown difference term and results in the Young–Dupré equation:

$$W_a = \gamma_{LV} \cdot (1 + \cos\vartheta) \tag{3}$$

which relates the measured contact angle to adhesion work. Traditionally, the work of solid-liquid adhesion has been determined through the measurement of contact angle. This contact angle based approach is very convenient and effective, however, it raises several theoretical and practical questions.

During a measurement cycle of capillary bridge probe, the capillary force is measured as a function of the change of bridge length that is as a function of the vertical displacement of the cylinder.

This work is only spent on changing the interfacial areas, if gravitational force is negligible. During approach and retraction, both the area of the liquid-vapor interface (A) and that of the solid-liquid interface (B) change. Consequently, the energy balance can be written as

$$-\int \vec{F} d\vec{z} = \Delta A \cdot \gamma_{LV} + \Delta B \cdot (\gamma_{SL} - \gamma_{SV}) \tag{4}$$

where $\vec{F}$ is the measured capillary force, $\vec{z}$ is the displacement of the cylinder, ΔA is the change of interfacial area between the liquid and vapor phase, and ΔB is the area change between the solid and the liquid, see Fig. 1. (The value of ΔA and ΔB are also dependent on the start and end points of the interval (z-range), over which the integration is performed.)

After rearranging Equation (4), the difference term in the bracket can be expressed as:

$$(\gamma_{SL} - \gamma_{SV}) - -\frac{\int \vec{F}\, d\vec{z} + \Delta A \cdot \gamma_{LV}}{\Delta B}. \tag{5}$$

One can substitute this experimentally otherwise unattainable term into the definition of adhesion work (Eq. (1)). Furthermore, considering that the net force and the displacement have only z-component, the vector notation can be omitted.

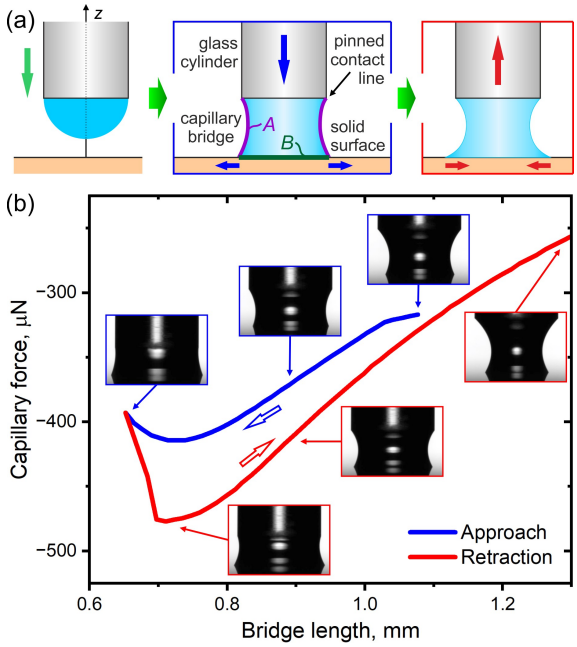

Figure 1. (a) *Schematics of the measurement steps. The liquid bridge is formed from a pedant drop. The contact line advances and recedes on the investigated surface, as the bridge length is decreased and then increased. During the length change, the image of the liquid bridge is captured and the capillary force is measured. The z axis is the axis of cylindrical symmetry.* ***(b)*** *Capillary force as a function of the bridge length measured on a hydrophilic (Si_3N_4) surface. The insets show captured images of the water capillary bridge. The diameter of the cylinder is 2 mm.*

This resulting formula gives the value of the solid-liquid adhesion work without the need of including any contact angle in the equation:

$$W_a = \gamma_{LV} + \frac{\int F\,dz + \Delta A \cdot \gamma_{LV}}{\Delta B} \quad . \tag{6}$$

Integration between the start and end points of approach and retraction gives the mechanical work done in the advancing and receding phases, respectively. The change of interfacial areas can be determined by simple image analysis in cylindrically symmetric case. Therefore, the solid-liquid adhesion work can be calculated according to Equation (6) for both the advancing and receding contact lines.

In conclusion, there is a century-old need for directly measured adhesion work values. The method determines the solid-liquid adhesion work directly and both for advancing and receding scenarios without any model assumptions. In advancing situation, the adhesion work quantifies the driving force behind spreading, while it gives the work required to remove the liquid from a unit of solid surface in receding case. The presented method provides an absolute, thermodynamic quantity, hence it is insensitive to the measurement parameters, and furthermore the resulting values can be used directly for further calculations, e.g. in the various surface free energy models. The method can be applied easily using commercial tensiometers equipped with an optional commercial camera module or with a laboratory-built one.

References:

[1] N. Nagy "Determination of solid-liquid adhesion work on flat surfaces in a direct and absolute manner" *Scientific Reports*, 14:29991 2024. [https://doi.org/10.1038/s41598-024-81710-6]
[2] N. Nagy „Eljárás és berendezés folyadék-szilárd adhéziós munka meghatározására" *Hungarian patent* (231 506)
[3] N. Nagy „Method and Apparatus for Determining Liquid-Solid Adhesion Work", *WIPO PCT patent application* (WO2023094846) [https://patentscope.wipo.int/search/en/detail.jsf?docId=WO2023094846]

Acknowledgement:

Support of Hungarian Sci.Research Fund OTKA FK 128901; TKP479 2021-EGA04 is acknowledged.

Optimized Sensing on Gold Nanoparticles Created by Graded-Layer Magnetron Sputtering and Annealing

D. Mukherjee[1, 2], K. Kertész[1], Z. Zolnai[1], Z. Kovács[1], A. Deák[1], A. Pálinkás[1], Z. Osváth[1], D. Olasz[1, 3], A. Romanenko[1,4], M. Fried[1, 2], S. Burger5, G. Sáfrán[1], P. Petrik[1,6]

[1]*Institute of Technical Physics and Materials Science, HUN-REN Centre for Energy Research, Konkoly Thege Str. 29–33, Budapest, 1121, Hungary*

[2]*Doctoral School of Materials Sciences and Technologies, Óbuda University, Népszínház u. 8, Budapest, 1081, Hungary*

[3]*Department of Materials Physics, Eötvös Loránd University, Pázmány Péter Sétány 1/A, Budapest, 1117, Hungary*

[4]*Doctoral School of Chemistry, Eötvös Loránd University, Pázmány Péter sétány 1/A, Budapest, H-1117, Hungary*

[5]*Zuse Institute Berlin (ZIB) & JCMwave GmbH, Takustraße 7, Berlin, 14195, Germany*

[6]*Department of Electrical Engineering, Institute of Physics, Faculty of Science and Technology, University of Debrecen, Bem tér 18, Debrecen, 4026, Hungary*

Gold nanoparticles (GNPs) possess optical properties making them especially suitable for plasmonic sensing. They are less than pristine, however, when it comes to the most common methods for fabricating them. These methodologies—electrochemical deposition, chemical methods, and physical vapor deposition—almost always yield GNPs with a uniform layer of gold. We know from working with metal nanoparticles in general that the optical properties of a particle are not just a function of the material, but also of its structure. That is why this work aims to methodically vary the deposition thickness, and the subsequent annealing (heating) of the deposited material to explore the three-dimensional structural evolution of GNPs [1,2]. The GNPs produced because of these explorations have been used to perform a series of optical characterizations that themselves serve as a basis for understanding the appearance and disappearance of the GNPs' optical sensing capabilities.

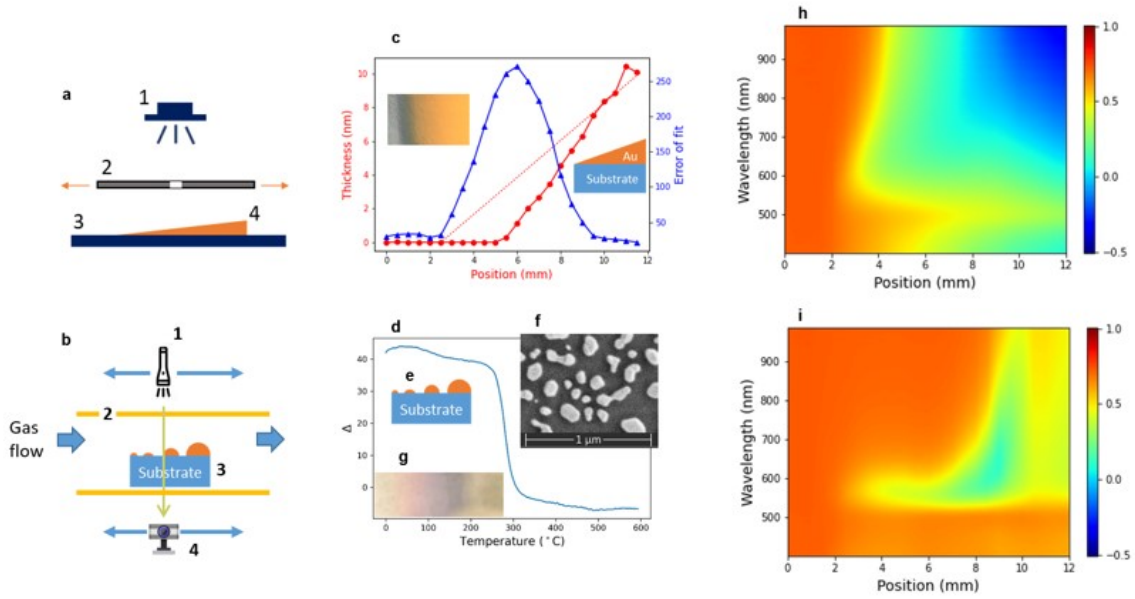

Figure 1: *(a) Schematic view of the micro-combinatorial sputtering method [4] (b) Configuration of the optical transmission cell. (c) Thickness (red circles), effective thickness [5] corresponding to the deposited amount of material (dotted line), and error of fit for the as-deposited graded Au sample measured by ellipsometry. (d) Change of Δ measured by ellipsometry as a function of temperature during annealing at the λ = 632.9 nm and position of 8 mm on sample (e) Schematic, (f) SEM (at a position of 8 mm), and (g) optical images on the sample after annealing. (h) and (i) show m33 spectra on sample over the range of positions from 0 to 12 mm for the as deposited and 300 ◦C annealed state, respectively.*

A graded-layer deposition approach was employed, where gold thickness varied from 0 to 20 nm across the substrate. After thermal annealing, the gold layers self-assembled into nanoparticles, forming distinct size and spacing distributions along the substrate [3]. At thin deposited layers (~1–2 nm), the nanoparticles were small and well-dispersed. At 3–7 nm, the particles coalesced into interconnected island-like structures. Beyond 7 nm, a continuous gold film formed, and the plasmonic properties of the system were reduced (Fig. 1). Scanning electron microscopy (SEM) was used to confirm that the mass thickness of deposition affected particle shape: the particle shape transitioned from oblate to hemispherical as thickness (and deposited mass) increased, affecting the near-field optics. The electron oscillation that resulted in the appearance of the local surface plasmon resonance (LSPR) peak was timelined to the onset of a hydrodynamic regime in finite element method (FEM) calculations [6]. Ellipsometry and transmission spectroscopy were used to analyse the optical response of the layers. The LSPR effect was observed, where electrons oscillated collectively at specific wavelengths depending on nanoparticle size and spacing. The LSPR peak appeared at ~550–600 nm for thinner layers (2–4 nm effective thickness). For thicker layers (>7 nm), LSPR diminished, indicating a loss of discrete plasmonic behaviour (Fig. 2). The experimental results were validated by FEM simulations predicting similar trends.

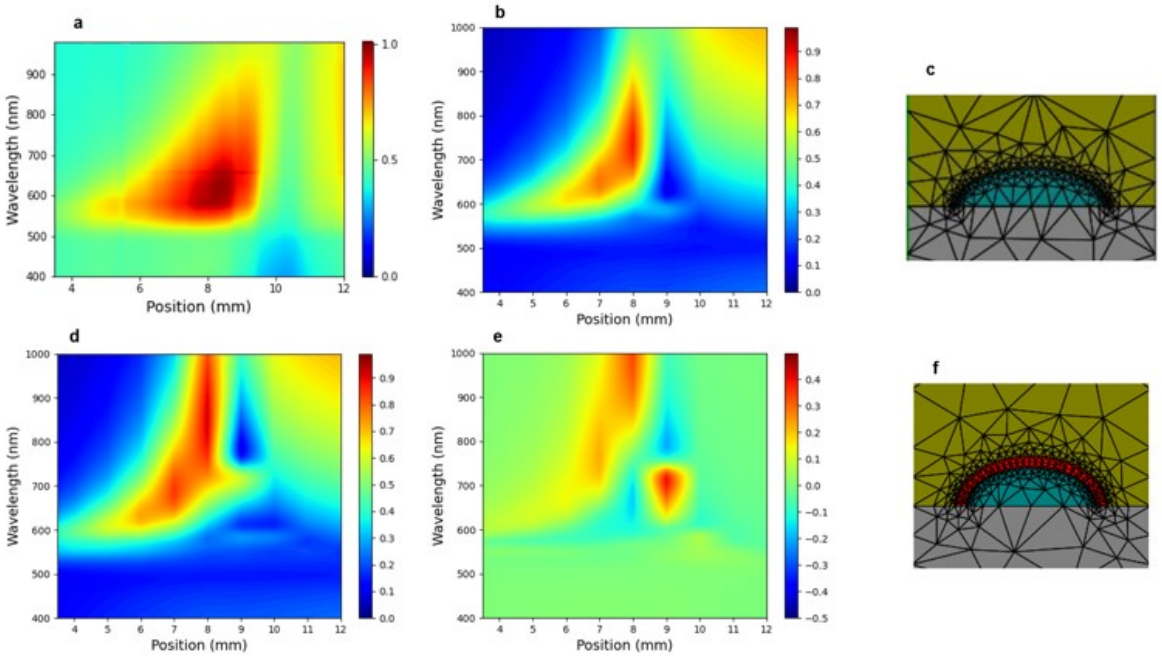

Figure 2: *Reflectance spectra measured along the sample and (b) simulated at normal incidence using (c) a FEM model. (d) Reflectance spectra calculated for the same structure with (f) a model using an overlayer with a thickness of 2 nm and $n=1.45+0.01/\lambda^2$, where the unit of λ is in µm. The differences between (b) and (d) are plotted in (e).*

We also conducted systematic evaluations of ethanol, water, and Raman reporter molecules as test analytes, correlating sensing efficiency with the deposited gold thickness and nanoparticle morphology. Optical transmittance spectroscopy was used to show that the refractive index altered upon ethanol and water adsorption, shifting the LSPR peak accordingly [7]. The best performance was recorded at a gold thickness of ~3.2 nm. This was the transition region where the nanoparticles were still discrete but had strong plasmonic coupling. Above ~ 7 nm, the sensing capability declined, as we moved into a region that behaved more like bulk gold and had less plasmonic enhancement. Surface-enhanced Raman Spectroscopy (SERS) was then used to probe our system and to see if we could take advantage of the intense electric fields to observe molecular signals. The most intense signals were recorded at 1.6-2 nm gold thickness, under the same conditions where we were getting near-field enhancement. The interparticle gap, most importantly its ratio to the particle size, was also critical.

FEM calculations were performed to model the optical responses of gold gratings under various conditions. We were able to successfully corroborate with the simulations the limits of detection based on the geometry of the nanoparticles and the changes in refractive index. We confirmed the shifts in the LSPR peak as a function of the size, spacing, and environmental refractive index of the nanoparticles, along with the surface coverage effects on resonance behaviour and the enhancement factors for SERS-based molecular detection. This research demonstrated that the combinatorial

sputtering technique can theoretically be applied to the scalable, precise, and reproducible fabrication of optimized gas and molecular sensors based on plasmonic structures. Optimized gold nanoparticle thicknesses of about 2-3 nm offered the best overall performance. These research findings also have implications for bimolecular (virus, protein) detection applications. Therefore, the anisotropic control of the GNPs along with the precise control of the gap widths significantly enhances the gas and molecular detection capabilities of the plasmonic sensors.

References:

[1] R.S. Moirangthem, Y.-C. Chang, P.-K. Wei, Ellipsometry study on gold- nanoparticle-coated gold thin film for biosensing application, Biomed. Opt. Express **(2011)** 2569.

[2] S. Kim, S. Park, S. Park, C. Lee, Acetone sensing of Au and Pd-decorated WO3 nanorod sensors, Sensors Actuators B 209 **(2015)** 180.

[3] B. Kalas, Z. Zolnai, G. Sáfrán, M. Serényi, E. Agocs, T. Lohner, A. Nemeth, N.Q. Khánh, M. Fried, P. Petrik, Micro-combinatorial sampling of the optical properties of hydrogenated amorphous Si1−xGex for the entire range of compositions towards a database for optoelectronics, Sci. Rep. 10 **(2020)** 19266.

[4] G. Sáfrán, ‘‘One-sample concept’’ micro-combinatory for high throughput TEM of binary films, Ultramicroscopy 187 **(2018)** 50.

[5] M. Loncaric, J. Sancho-Parramon, H. Zorc, Optical properties of gold island films—a spectroscopic ellipsometry study, Thin Solid Films 519 **(2011)** 2946.

[6] F. Binkowski, T. Wu, P. Lalanne, S. Burger, A.O. Govorov, Hot electron generation through near-field excitation of plasmonic nanoresonators, ACS Photonics 8 **(2021)** 1243.

[7] M. Kang, S.-G. Park, K.-H. Jeong, Repeated solid-state dewetting of thin gold films for nanogap-rich plasmonic nanoislands, Sci. Rep. 5 **(2015)** 14790.

Acknowledgement:

Support of Hungarian Sci.Research Fund TKP EGA-04, OTKA K 131515, EMPIR POLight is acknowledged.